Review

Single-Photon Detectors for Quantum Integrated Photonics

Thu Ha Dao [1,*], Francesco Amanti [2], Greta Andrini [3,4], Fabrizio Armani [5], Fabrizio Barbato [3], Vittorio Bellani [6,7], Vincenzo Bonaiuto [1,8], Simone Cammarata [2,9], Matteo Campostrini [10], Samuele Cornia [7,11], Fabio De Matteis [1,8], Valeria Demontis [7,12,13], Giovanni Di Giuseppe [14,15], Sviatoslav Ditalia Tchernij [4,16], Simone Donati [2,17], Andrea Fontana [7], Jacopo Forneris [4,16], Roberto Francini [1,8], Luca Frontini [5,18], Gian Carlo Gazzadi [19], Roberto Gunnella [14,16], Ali Emre Kaplan [20], Cosimo Lacava [7,21], Valentino Liberali [5,18], Leonardo Martini [7,11], Francesco Marzioni [14,15,22], Claudia Menozzi [11], Elena Nieto Hernández [4,16], Elena Pedreschi [2], Paolo Piergentili [14,15], Paolo Prosposito [1,8], Valentino Rigato [10], Carlo Roncolato [10], Francesco Rossella [7,11], Matteo Salvato [23], Fausto Sargeni [1,24], Jafar Shojaii [25], Franco Spinella [2], Alberto Stabile [5,18], Alessandra Toncelli [2,17], Gabriella Trucco [5,26] and Valerio Vitali [7,21]

1 Sezione di Roma Tor Vergata, Istituto Nazionale di Fisica Nucleare, 00133 Roma, Italy; vincenzo.bonaiuto@uniroma2.it (V.B.); fabio.dematteis@roma2.infn.it (F.D.M.); francini@roma2.infn.it (R.F.); paolo.prosposito@uniroma2.it (P.P.); fausto.sargeni@roma2.infn.it (F.S.)
2 Sezione di Pisa, Istituto Nazionale di Fisica Nucleare, 56127 Pisa, Italy; francesco.amanti@pi.infn.it (F.A.); simone.cammarata@phd.unipi.it (S.C.); simone.donati@unipi.it (S.D.); elena.pedreschi@pi.infn.it (E.P.); franco.spinella@pi.infn.it (F.S.); alessandra.toncelli@unipi.it (A.T.)
3 Dipartimento di Elettronica e Telecomunicazioni, Politecnico di Torino, 10129 Torino, Italy; greta.andrini@polito.it (G.A.); fabrizio.barbato@pi.infn.it (F.B.)
4 Sezione di Torino, Istituto Nazionale di Fisica Nucleare, 10125 Torino, Italy; sviatoslav.ditaliatchernij@unito.it (S.D.T.); jacopo.forneris@unito.it (J.F.); elena.nietohernandez@unito.it (E.N.H.)
5 Sezione di Milano, Istituto Nazionale di Fisica Nucleare, 20133 Milano, Italy; fbarm@tutanota.com (F.A.); luca.frontini@mi.infn.it (L.F.); valentino.liberali@mi.infn.it (V.L.); alberto.stabile@mi.infn.it (A.S.); gabriella.trucco@mi.infn.it (G.T.)
6 Dipartimento di Fisica, Università di Pavia, 27100 Pavia, Italy; vittorio.bellani@unipv.it
7 Sezione di Pavia, Istituto Nazionale di Fisica Nucleare, Via Agostino Bassi 6, 27100 Pavia, Italy; samuele.cornia@gmail.com (S.C.); valeria.demontis@sns.it (V.D.); andrea.fontana@pv.infn.it (A.F.); cosimo.lacava@unipv.it (C.L.); leonardo.martini@unimore.it (L.M.); francesco.rossella@unimore.it (F.R.); valerio.vitali@unipv.it (V.V.)
8 Dipartimento di Ingegneria Industriale, Università di Roma Tor Vergata, 00133 Roma, Italy
9 Dipartimento di Ingegneria dell'Informazione, Università di Pisa, 56122 Pisa, Italy
10 Laboratori Nazionali di Legnaro, Istituto Nazionale di Fisica Nucleare, 35020 Legnaro, Italy; matteo.campostrini@lnl.infn.it (M.C.); valentino.rigato@lnl.infn.it (V.R.); carlo.roncolato@lnl.infn.it (C.R.)
11 Dipartimento di Scienze Fisiche, Informatiche e Matematiche, Università di Modena e Reggio Emilia, 41125 Modena, Italy; claudia.menozzi@unimore.it
12 National Enterprise for nanoScience and nanoTechnology, Scuola Normale Superiore, Istituto Nanoscienze—Consiglio Nazionale delle Ricerche, 56127 Pisa, Italy
13 Dipartimento di Fisica, Università di Cagliari, 09124 Cagliari, Italy
14 Scuola di Scienze e Tecnologie, Divisione di Fisica, Università di Camerino, 62032 Camerino, Italy; gianni.digiuseppe@unicam.it (G.D.G.); roberto.gunnella@unicam.it (R.G.); francesco.marzioni@unicam.it (F.M.); paolo.piergentili@unicam.it (P.P.)
15 Sezione di Perugia, Istituto Nazionale di Fisica Nucleare, 06123 Perugia, Italy
16 Dipartimento di Fisica, Università di Torino, 10125 Torino, Italy
17 Dipartimento di Fisica, Università di Pisa, 56127 Pisa, Italy
18 Dipartimento di Fisica, Università di Milano, 20133 Milano, Italy
19 Istituto Nanoscienze—Centro S3, Consiglio Nazionale delle Ricerche, Via Campi 213/A, 41125 Modena, Italy; giancarlo.gazzadi@nano.cnr.it
20 Optoelectronics Research Center, University of Southampton, Southampton SO17 1BJ, UK
21 Dipartimento di Ingegneria Industriale e dell'Informazione, Università di Pavia, 27100 Pavia, Italy
22 Dipartimento di Fisica, Università di Napoli "Federico II", 80126 Napoli, Italy
23 Dipartimento di Fisica, Università di Roma Tor Vergata, 00133 Roma, Italy; matteo.salvato@roma2.infn.it
24 Dipartimento di Ingegneria Elettronica, Università di Roma Tor Vergata, 00133 Roma, Italy
25 Space Technology and Industry Institute, Swinburne University of Technology, Hawthorn, VIC 3122, Australia; jshojaii@swin.edu.au

26   Dipartimento di Informatica, Università di Milano, 20133 Milano, Italy
*   Correspondence: tdao@roma2.infn.it

Abstract: Single-photon detectors have gained significant attention recently, driven by advancements in quantum information technology. Applications such as quantum key distribution, quantum cryptography, and quantum computation demand the ability to detect individual quanta of light and distinguish between single-photon states and multi-photon states, particularly when operating within waveguide systems. Although single-photon detector fabrication has been established for some time, integrating detectors with waveguides using new materials with suitable structural and electronic properties, especially at telecommunication wavelengths, creates more compact source-line-detector systems. This review explores the state of the art of single-photon detector research and examines the potential breakthroughs offered by novel low-dimensional materials in this field.

1. Introduction

Since the 1980s, significant advancements have been made in understanding how quantum mechanics can be applied to solve practical problems, such as developing a computer that operates based on quantum principles. In recent years, efforts have been focused on creating quantum information and computation platforms that are compatible with digital and telecommunications technologies without requiring a cryogenic environment. The current state of research in quantum integrated photonics is reviewed in Ref. [1], highlighting the most widely used integrated photonic platforms and summarizing key achievements and results from the past decade. Integrated photonics on Silicon-On-Insulator (SOI) substrates has become a well-established field of research with significant impact, particularly in quantum computing. Despite the potential to create highly complex circuits using this technology, the foundation remains a set of fundamental "building blocks" that are combined to form intricate designs. Ref. [2] provides a comprehensive review of the current state of integrated photonic building blocks, focusing specifically on passive elements. It explores the fundamental principles and design methodologies that are essential for constructing these components and advancing the field further. In [3], one can find the latest endeavors in hybrid photonic platforms leveraging the combination of integrated silicon photonic platforms and nanoscale materials, allowing for the unlocking of increased device efficiency and compact form factors. Moreover, the review provides insights into future developments and the evolving landscape of hybrid integrated photonic nanomaterial platforms. The quest for reliable and integrable single-photon sources (popular approaches include spanning cold atoms and ions [4], quantum dots [5,6], isolated molecules [7], color centers in the solid state [8]), and single-photon detectors (SPD) is at the center of the research efforts in the field.

A photon is defined as the elementary excitation of a single mode of the quantized electromagnetic field [9]. This fundamental particle exhibits characteristics of both particles and waves, serving as a discrete quantum of electromagnetic radiation. Photons are characterized by their frequency, with a single photon in a specific mode having an energy equal to Planck's constant (h) multiplied by the frequency (ν) of that mode. Despite their often-described monochromatic nature, practical applications involve "single-photon states" that can be mathematically described as superpositions of monochromatic photon modes, allowing for considerations of their localization in time and space. These particles

are integral to the foundations of quantum mechanics and find extensive applications in various fields, including quantum information science and quantum communication. In the context of single-photon detectors, a photon is considered a discrete particle of light that can be individually detected by the single-photon detector.

The contemporary surge in detector research is significantly propelled by the exponential growth of the field of quantum information science in recent decades [10,11]. Fundamentally, quantum information science revolves around the encoding, communication, manipulation, and measurement of information through quantum-mechanical entities. Studies in this domain have revealed that the employing of quantum objects for these purposes enables the execution of specific computational tasks with greater efficiency than previously believed possible with classical counterparts [12]. Furthermore, it has the potential to enable unconditionally secure communication [13]. In this context, photonic qubits stand out as a preferred choice for numerous applications. These qubits encode information in the quantum state of a photon, utilizing various degrees of freedom such as polarization, momentum, and energy. Photonic qubits prove advantageous for several reasons. First, photons travel at the speed of light and exhibit weak interactions with their environment over extended distances. This characteristic results in reduced noise and loss during information transmission. Second, photons can be adeptly manipulated using linear optics, enhancing their suitability for diverse quantum information-processing tasks. These unique attributes render photonic qubits exceptionally promising for advancing the frontier of quantum information science.

Quantum communication applications, particularly those involving quantum key distribution (QKD) protocols, frequently rely on single photons. In the realm of quantum cryptography, especially in the context of QKD, the requirement for single photons traveling through a channel is paramount. This strict adherence to single-photon transmission is crucial due to the vulnerability introduced by the presence of multiple photons, which could potentially compromise the security of communication by allowing eavesdroppers to gain unauthorized access to information [13–17]. The field of quantum computation necessitates the use of single photons, with an additional requirement that all single photons utilized in the protocols be indistinguishable from each other [18]. Consequently, the utilization of single-photon detectors capable of accurately determining the number of photons within a given pulse becomes imperative in these contexts. Moreover, the significance of single-photon detection extends to the generation of truly random numbers, a vital requirement not only in quantum cryptography but also in various non-quantum-related fields. In this context, light offers a natural solution, where single photons encountering a beam-splitter exhibit inherent quantum randomness in choosing their output path [19–21]. Extracting this path information relies on the precise detection of single photons, making single-photon detectors indispensable in the production of genuinely random numbers, a requirement emerging from quantum key distribution protocols and finding applications beyond the realm of quantum physics. The history of single-photon detectors for quantum information processing is marked by significant milestones shown in Figure 1. Throughout this history, the synergy between theoretical advancements in quantum information science and practical developments in detector technology has driven the field forward, enabling the realization of various quantum communication and computation protocols. The use of SPDs to support high-speed QKD at speeds of 10 to 100 Mbps represents a significant advancement in quantum communication technologies [22,23]. Achieving such high data rates requires overcoming the traditional challenges of photon detection, including timing precision, detection efficiency, and noise suppression. SPDs are also critical for other quantum communication paradigms (such as secure quantum direct communication [24]) and many other fields. In quantum sensing, SPDs enable applications such as quantum imaging,

where they capture high-resolution images using entangled photons; quantum LiDAR (light detection and ranging), which leverages time-of-flight measurements for precise depth mapping; and quantum metrology, where they enhance sensitivity in interferometric measurements for gravitational wave detection and atomic clocks. In quantum communication, SPDs are integral to QKD, enabling secure encryption with high-speed detection rates. They are also crucial in satellite-based QKD, quantum repeaters for long-distance networks, and the verification of quantum states such as entanglement in quantum networking. SPDs are instrumental in quantum secure time synchronization (QSTS), enabling precise alignment of clocks in distributed systems by leveraging the properties of single-photon-level signals. In QSTS protocols, SPDs detect time-correlated photons to synchronize clocks with picosecond-level precision, ensuring robust security against eavesdropping. This capability is vital for applications in quantum networks, secure communications, and distributed quantum computing. SPDs are essential components in quantum computing, enabling precise measurement and control of quantum states critical to computation and communication tasks. They are used in photonic quantum computing to detect and manipulate individual photons in quantum circuits, ensuring high-fidelity operations in processes like entanglement generation and state teleportation. In this review, we focus on technologies that can be integrated into an on-chip configuration.
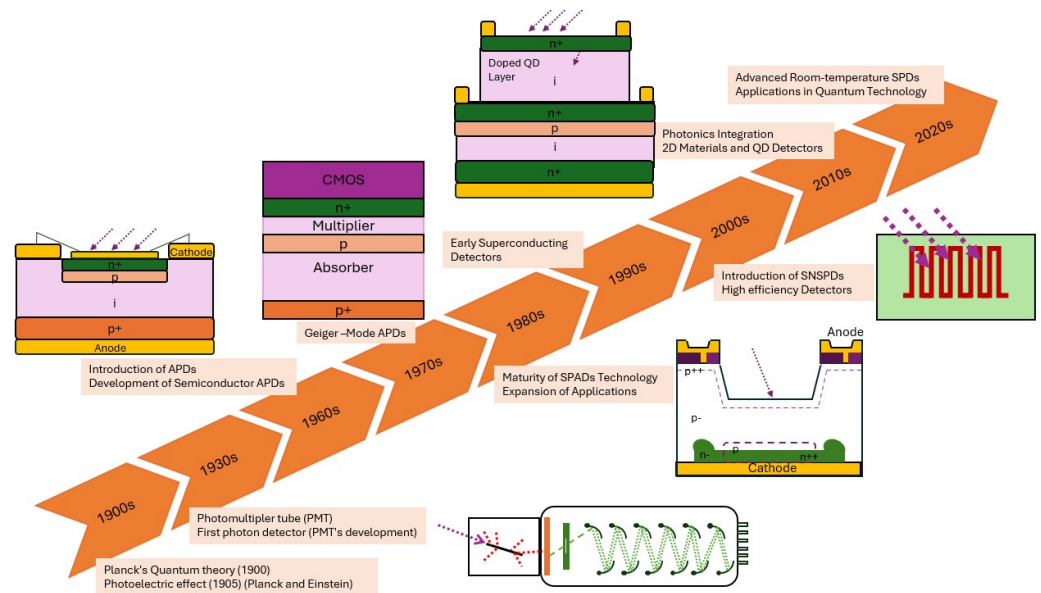

Figure 1. Brief history of single-photon detectors.

2. Properties of Single-Photon Detector

Single-photon detectors possess specific properties that make them well-suited for applications requiring the detection and measurement of individual photons. Here are some key properties of single-photon detectors:

Quantum Efficiency: quantum efficiency refers to the probability that a detector will register a photon that impinges upon it. High quantum efficiency is crucial for maximizing the chances of detecting individual photons.

Detection Efficiency: detection efficiency is a measure of the actual detection rate of a detector compared to the number of photons incident upon it. It accounts for factors such as quantum efficiency, dark counts, and other losses.

Noise Levels: single-photon detectors should have low noise levels to ensure accurate and reliable detection of individual photons. Noise can arise from various sources, including thermal effects and electronic components.

Efficiency at Specific Wavelengths: some detectors are optimized for specific wavelengths, providing higher efficiency and sensitivity within a particular range. This is crucial in applications such as telecommunications and quantum optics.

Photon-Number Resolution: in certain applications, it is essential to determine the number of photons in an incident pulse accurately. Single-photon detectors with photon-number-resolving capabilities can distinguish between different photon numbers.

Timing jitter: refers to the uncertainty or variation in the exact moment when the detector registers a photon after its arrival. It is a measure of the temporal precision of the detector and is critical for applications requiring accurate timing, such as quantum communication, time-of-flight measurements, and time-resolved spectroscopy. The timing jitter is typically expressed as the full width at half maximum (FWHM) of the distribution of detection times. Timing jitter arises from various factors, including the inherent response time of the detector material, the stochastic nature of carrier multiplication (as in avalanche photodiodes), and the noise or delays introduced by signal processing electronics.

Operational Temperature: some detectors, such as superconducting detectors, operate at low temperatures to enhance their performance. The operational temperature can impact various properties of the detector.

Spectral Range: a photon counter's sensitivity is limited to a specific spectral range determined by the materials of which it is composed. The choice of the operating wavelength depends on the specific application at hand. In the context of free-space optical applications, including both bench-top quantum optics experiments [25] and line-of-sight QKD conducted through the atmosphere [19], visible or near-infrared wavelengths are typically employed. This choice is driven by the availability of the best commercially accessible detectors in these spectral regions. In optical fiber systems, losses are minimized at a wavelength of 1550 nm, making it the preferred choice for long-distance QKD applications within optical fibers [19]. Moreover, advanced optical components such as on-chip waveguides are specifically engineered for telecommunications wavelengths. Consequently, there exists substantial interest within the quantum information field in the development and utilization of detectors sensitive to telecommunications wavelength photons. This interest is primarily fueled by the compatibility of such detectors with various QI applications, especially those integrated into existing telecommunications infrastructures.

Dead time: the parameter known as "dead time", denoted as τ, represents the time interval following the absorption of a photon during which the detector is incapable of reliably registering a subsequent photon. The specific duration of τ is contingent upon the type of detector in use and is influenced by various factors unique to each detector type. It is noteworthy that in many instances, the measured value of τ pertains to the characteristics of the bias circuit or the counting electronics rather than the inherent properties of the detector element itself.

In the case of semiconductor single-photon detectors, τ is intentionally prolonged to mitigate afterpulsing—a phenomenon wherein the detector spontaneously re-triggers after an initial detection event. By lengthening τ, afterpulsing can be suppressed effectively. It is imperative to acknowledge that the dead time imposes a constraint on the maximum count rate achievable by the detector. However, it does not impose limitations on the clock rate of the experiment. In practice, time-correlated single-photon counting (TCSPC) experiments are typically conducted in a regime where the number of detected photons per clock cycle remains significantly below one, allowing for higher clock rates in the experimental setup. This strategic operation ensures optimal efficiency and accuracy in photon detection processes.

Dark-Count rate: refers to false detection events that occur without any actual photons entering the detector. These events can be classified into fundamental dark counts and

background counts. Fundamental dark counts originate from intrinsic properties of the detector, such as thermal noise, where thermally generated carriers or quantum tunneling of electrons can cause spurious detections. Afterpulsing, where residual charge from previous detections triggers false counts, is another key factor. These counts are typically minimized through cooling or design optimization. Background counts, on the other hand, result from external sources of electromagnetic radiation, such as ambient light, cosmic rays, or infrared radiation from surrounding objects. These can be reduced through proper shielding and filtering. Understanding the balance between these two types of dark counts is crucial for optimizing detector performance in applications like quantum communication and sensing, where minimizing false counts is vital for accurate measurements and secure transmissions. The dark-count rate, represented in s^{-1}, or the derived unit hertz Hz (one Hz is one per second or the reciprocal of one second), characterizes the frequency of these false counts. However, techniques such as gating or time-stamping the detection events can be employed to mitigate the impact of dark counts. It is crucial to note that the minimum time interval for implementing gating or time-stamping is dictated by the timing jitter inherent to the detector. This constraint emphasizes the importance of considering the detector's inherent characteristics when implementing strategies to address the issue of dark counts in practical applications.

Linearity: refers to the proportional relationship between the number of incident photons and the detector's output signal. A highly linear detector will produce an output that scales consistently with the number of photons over a given range, making it suitable for applications requiring quantification of photon flux, such as fluorescence imaging or multi-photon spectroscopy. Linearity ensures that the detector can faithfully represent variations in photon intensity without saturation or distortion.

SPDs rely on several key parameters that are inherently interdependent, often requiring trade-offs to optimize performance for specific applications. One fundamental trade-off is between detection efficiency (DE) and dark-count rate (DCR). High DE, which indicates the probability of successfully detecting an incident photon, often requires increasing bias voltage or enhancing photon absorption. However, these measures can also elevate the DCR due to noise from thermal or tunneling effects. Cryogenic cooling can help suppress the DCR but may slightly reduce DE in some materials by altering their detection efficiency. Another critical relationship is between timing jitter and DE. Timing jitter measures the uncertainty in the detection timing, which is crucial for applications like quantum communication. Enhancing DE often involves optimizing absorption and avalanche mechanisms, potentially extending the timing window and increasing jitter. Conversely, reducing jitter requires precise amplification and noise filtering, which can slightly reduce DE. The relationship between operational temperature, DCR, and DE is also pivotal. Lowering the temperature reduces thermal noise, effectively suppressing the DCR, but can add system complexity and impact DE in some designs. Speed and efficiency represent another trade-off in SPDs. Higher speed, defined by shorter dead times, allows detectors to register consecutive photons rapidly. However, achieving high speed often requires optimizing quenching mechanisms, which can reduce DE. For example, avalanche-based SPDs face challenges in balancing rapid reset times with the efficiency of photon detection. Superconducting nanowire SPDs (SNSPDs) achieve exceptional speed but at the cost of requiring advanced cryogenic technologies. Lastly, linearity and photon-number resolution often conflict in SPDs. Linearity refers to the detector's ability to scale output proportionally with photon number, while photon-number resolution is the capability to distinguish between different numbers of incident photons. Detectors optimized for high photon flux may lose the ability to resolve single photons accurately. These interdependencies must be carefully managed to meet the requirements of specific applications, such as

quantum key distribution, biological imaging, or integrated photonics. Optimizing SPDs for one parameter often involves compromises in others, necessitating a tailored approach to design and operation.

3. Approaches to Single-Photon Detector

A photon-number-resolving (PNR) detector generates an output that directly correlates with the number of photons entering the detector within a specific range. This allows for determining an integer count of detected photons, typically with a high precision and minimal uncertainty. These detectors are sometimes termed "intrinsic photon-number-resolving detectors" to differentiate them from quasi-PNR detectors. Non-photon-number-resolving (non-PNR) detectors function primarily by distinguishing between the presence or absence of photons based on a defined detection threshold. These devices do not provide information about the precise number of photons detected. Often, such detectors are referred to as "click detectors", "click/no-click detectors", "on/off detectors", or "threshold detectors". A quasi-photon-number-resolving (quasi-PNR) detector utilizes temporally and/or spatially multiplexed detectors—such as a detector array or a beamsplitter-detector tree—each of which lacks individual photon-number-resolving capability. The effectiveness of such systems, including their n-photon efficiency, can be influenced by this limitation. These systems are most effective when the number of incident photons is significantly lower than the number of multiplexed detectors.

The categorization of detectors into photon-number-resolving and non-photon-number-resolving types is not always straightforward. Some detectors, initially classified as non-photon-number-resolving, exhibit partial photon-number-resolving capabilities, while continuous efforts are made to enhance or incorporate this capability into detectors lacking it. Conversely, detectors classified as photon-number-resolving may not accurately determine the true number of incident photons if their efficiency is less than perfect. Furthermore, the presence of dark counts further compounds the disparity between the measured outcome and the actual number of incident photons. This complexity highlights the challenges involved in accurately characterizing the photon-number resolution capabilities of detectors, emphasizing the need for detailed evaluation and continuous advancements in detector technology.

3.1. Single-Photon Avalanche Diodes (SPADs)

Avalanche photodetectors (APDs) represent highly sensitive semiconductor photodiode detectors that harness the photoelectric effect to convert light into electrical signals. Functionally, they can be considered to be the semiconductor counterparts to photomultiplier tubes, renowned for their sensitivity and efficiency in detecting photons. The concept of the APD was pioneered by Japanese engineer Jun-ichi Nishizawa in 1952 [26], although prior research delved into avalanche breakdown phenomena, micro-plasma defects in silicon and germanium, as well as optical detection using p-n junctions. APDs find diverse applications in various fields. They are commonly utilized in laser rangefinders, long-range fiber-optic telecommunication systems, and quantum sensing applications, where they play a crucial role in control algorithms. Moreover, emerging applications include their usage in positron emission tomography and particle physics experiments, showcasing the versatility and significance of APDs in advancing scientific research and technological innovation.

Semiconductor materials play a crucial role in the performance and application of APDs. Different materials offer varying detection capabilities and noise characteristics, making them suitable for specific wavelength ranges and applications. Each of these semiconductor materials possesses distinct optical and noise characteristics, enabling their utilization across a broad range of wavelengths and specialized applications in the realm of APDs (Table 1).

Table 1. Semiconductor materials for APDs.

Material	WL (μm)	Noise	Breakdown Voltage (V)	PDE
Si	0.4–1.1	Low noise, high gain	~100–200	~80–90% (VIS)
Ge	0.8–1.6	Higher than Si	~50–100	~30–50% (NIR)
InGaAs	0.9–1.7	Low in NIR	~20–50	~50–70% (NIR)
GaN	0.2–0.4 (UV)	High in early models	>200	~40–60% (UV)
HgCdTe	1–14 (IR)	High (requires cooling)	5–15	>60% (IR)

WL: wavelength; PDE: photon detection efficiency.

The applicability and utility of APDs are contingent upon various parameters, with two significant factors being quantum efficiency and total leakage current. Quantum efficiency quantifies the efficiency with which incident optical photons are absorbed and subsequently utilized to generate primary charge carriers within the APD. On the other hand, total leakage current encompasses the cumulative effect of dark current, photocurrent, and noise components. Dark noise in APDs comprises to sources of noise. Series noise, influenced by shot noise, is directly proportional to the APD capacitance. In contrast, parallel noise is linked to fluctuations in the APD's bulk and surface dark currents. These noise components, alongside quantum efficiency and total leakage current, intricately determine the performance characteristics and limitations of APDs. Understanding and optimizing these parameters are essential for enhancing the reliability and effectiveness of APDs in various applications, ranging from telecommunications to scientific research.

SPADs employ a process akin to PMT but with distinctive features. When a photon is absorbed, it generates an electron-hole pair within the semiconductor lattice. Unlike PMTs, where charge multiplication occurs between discrete dynodes in a vacuum, SPADs operate in a continuous charge multiplication mode. In the Geiger mode, a bias voltage exceeding the diode's breakdown voltage is applied. In this mode, when a photon generates a charge, the avalanche proceeds until it saturates at a current, often limited by an external circuit. This current sustains itself, allowing the SPAD to respond to subsequent incoming optical pulses. However, the saturated avalanche current must be terminated by lowering the bias voltage below the breakdown voltage before the SPAD can detect another photon. It is important to note that the concept of gain is not applicable in Geiger mode due to the saturation phenomenon. Geiger-mode SPADs can achieve detection efficiencies surpassing those of PMTs, reaching up to 85% for silicon SPADs in the visible spectrum. The model reported in [27] achieved receiver sensitivity of −64 dBm with a 100 kbit/s signal at a bit error ratio of 10^{-5}. Future improvements in SPAD visible light communication receiver architecture are still required to approach the quantum limit. The disadvantage of SPADs is that they exhibit higher dark-count rates and timing jitter compared to the best PMTs. In the case of infrared (IR) SPADs, efficiencies typically range from 50% to 70%, with considerably higher dark-count rates than PMTs [28]. To mitigate dark-count rates, SPADs are commonly cooled using thermoelectric coolers to temperatures ranging from 210 K to 250 K, enhancing their performance in low-light conditions and enabling their application in various sensitive detection systems.

Moreover, the gain medium within SPADs typically contains trap sites that require time to depopulate after an avalanche event before the bias voltage can be restored. If these trap sites are not given adequate time to depopulate, a second avalanche can be

triggered by carriers released from the traps rather than by a new incoming photon. This phenomenon, known as "afterpulsing", necessitates an additional waiting period after each pulse before the device can be rebiased. Consequently, SPADs experience dead times ranging from tens of nanoseconds to 10 microseconds. This issue is particularly challenging for SPADs designed for IR sensitivity, where precise timing and accurate detection are crucial. Managing afterpulsing effects is essential for optimizing the performance of SPADs in IR applications, where high sensitivity and low noise are paramount requirements.

While the majority of commercial SPADs operate in Geiger mode, ongoing research efforts are directed toward developing linear-mode operation for photon counting. Linear-mode operation offers several advantages, including an output proportional to the number of incident photons, providing photon-number resolution. Additionally, it results in lower afterpulsing due to reduced current flow and diminished trap filling, along with reduced dead time. In linear mode, smaller current pulses are generated, necessitating longer measurement times to reduce readout noise. A recent demonstration achieved a 56% detection efficiency and a dark-count rate of 0.0008 s^{-1} at a maximum repetition rate of 10 kHz [29]. However, these linear devices face challenges related to noise on the gain and the smaller signals involved. This can lead to the broadening of the output current pulse amplitudes to an extent where pulses resulting from different numbers of incident photons cannot be reliably resolved. As of the latest information available, there have been no demonstrated instances of achieving precise photon-number resolution with these devices. Ongoing research in this area aims to address these challenges and unlock the full potential of linear-mode SPADs for applications demanding accurate photon-number resolution [30,31].

Table 2 provides a short comparison of various materials utilized in the fabrication of semiconductor SPADs. The work in[32] presents a new generation of planar germanium-on-silicon (Ge-on-Si) SPAD detectors designed for short-wave infrared applications. This planar geometry marks a significant advancement in performance, achieving a single-photon detection efficiency of 38% at 125 K and a wavelength of 1310 nm. Furthermore, it demonstrates a fifty-fold reduction in noise equivalent power compared to optimized mesa geometry SPADs, highlighting its superior operational capabilities.

Table 2. Semiconductor materials for SPADs.

Material	DCR (cps)	PDE	Breakdown Voltage (V)	Applications
Si	Low (~10–100)	~50–70% (VIS)	~20–30	Quantum imaging, LIDAR, fluorescence microscopy
Ge	Moderate (~10^3)	~10–30% (NIR)	~30–50	Telecom, NIR spectroscopy
InGaAs	Moderate (~10^3, cooled)	~40–60% (NIR)	~40–60	QKD, fiber optics
GaN	Moderate (~10^3)	~30–40% (UV)	>200	UV detection, flame monitoring
HgCdTe	High (cryogenic cooling)	~50–70% (IR)	~10–15	Thermal imaging, infrared astronomy

DCR: dark-count rate; PDE: photon detection efficiency.

The study in [33] describes the fabrication of a device with a thick InGaAs absorption region and an anti-reflection layer, achieving a quantum efficiency of 83.2%. The single-photon performance is evaluated using a quenching circuit that integrates parallel-balanced InGaAs/InP single-photon detectors and single-period sinusoidal pulse gating. The capacitance-induced spike pulse is suppressed through parallel-balanced common mode signal elimination, enabling the detection of small avalanche pulse amplitude signals. The device demonstrates a maximum detection efficiency of 55.4%, a dark-count rate of 43.8 kHz, and a noise equivalent power of 6.96×10^{-17} W/Hz$^{1/2}$ at 247 K.

The paper [34] reports on performance enhancements for near-infrared single-photon detectors achieved through the implementation of a novel reflector design, which integrates a metal layer and a SiO$_2$/TiO$_2$ distributed Bragg reflector. Additionally, a micro-lens is

incorporated, increasing absorption efficiency by 58%. The device demonstrates normalized dark-count rates of 127 Hz, 361 Hz, and 665 Hz for photon detection efficiencies of 10%, 20%, and 30%, respectively, when operated in gated mode with a 50 MHz pulse repetition rate and 1 ns pulse width at a temperature of 233 K. These normalized dark-count rates are nearly an order of magnitude lower than those of commercial counterparts, underscoring the high performance of the proposed design.

The study in [35] introduces a novel InGaAs/InP SPAD structure fabricated using the selective area growth technique. The surface topography of the selectively grown film within 70 μm diffusion apertures is leveraged to engineer the Zn diffusion profile, effectively suppressing premature edge breakdown. This approach enables the creation of a highly uniform active area without requiring shallow diffused guard ring regions typically used in standard InGaAs/InP SPADs. The device achieves photon detection probabilities (PDP) of 33% and 43% at 1550 nm for 5 V and 7 V excess bias, respectively, with measurements conducted at 300 K and 225 K. At room temperature and 5 V excess bias, the DCR per unit area is 430 counts per second per μm^2, which decreases to 5 counts per second per μm^2 at 225 K. Timing jitter at 1550 nm is measured as 149 ps (FWHM) using passive quenching, under 300 K and 5 V excess bias conditions.

Maurice et al. [36] present experimental findings on Ge-on-Si SPADs employing a novel double-mesa structure. This design effectively suppresses the electric field at the mesa edges compared to conventional single-mesa configurations, leading to substantial performance enhancements. In linear mode, the double-mesa structure demonstrates a significantly smaller increase in dark current at higher reverse voltages, resulting in a reduction of over 260-fold at low temperatures. When operated in Geiger mode at 110 K, the dark-count rate is reduced by 100-fold. The device achieves a dark-count rate of 953 kHz, a single-photon detection efficiency of 7.3%, and an ultra-low timing jitter of 81 ps at an excess bias of 17.6% and a temperature of 110 K. This work highlights the potential of the double-mesa structure for high-performance SPAD applications.

Mew et al. [37] present the first experimental evaluation of $In_{0.53}Ga_{0.47}As/Al_{0.85}Ga_{0.15-}As_{0.56}Sb_{0.44}$ APDs operating in Geiger mode. Multiple devices were characterized, focusing on temperature-dependent dark current, avalanche multiplication, dark-count rate (DCR), afterpulsing, and single-photon detection efficiency (SPDE). The devices demonstrated a temperature coefficient of breakdown voltage of 13.5 mV/K, significantly lower than that of InGaAs/InP Geiger-mode APDs. This reduces operational voltage variations and potentially mitigates thermal attack risks in communication systems. At 200 K, SPDE ranged from 5% to 16% with DCR values of 1–20 Mc/s, comparable to InAlAs and early InP-based single-photon APDs. Afterpulsing was negligible with a hold-off time of >50 μs at 200 K, decreasing to 5 μs at 250 K. These results align with the performance of InGaAs/InAlAs and certain InGaAs/InP Geiger-mode APDs, underscoring the potential of this material system for single-photon detection applications.

The study in Ref. [38] introduces a waveguide-coupled Si SPAD integrated into a silicon photonic platform for operation in the visible spectrum. The device achieved a single-photon detection efficiency exceeding 6% at wavelengths of 488 nm and 532 nm, with an excess voltage below 20% of the breakdown voltage. At room temperature, the dark-count rate remained under 100 kHz, with a potential reduction of approximately 35% when the temperature was lowered to −5 °C. This advancement highlights the potential of silicon photonics for visible-wavelength single-photon detection applications.

The study in Ref. [39] presents a CMOS-compatible, high-performance GE-Si SPAD operated at room temperature. The device demonstrated a dark-count rate of 19 kHz μm^{-2}, a single-photon detection probability of 12% at 1310 nm, and a timing jitter of 188 ps. Additionally, the afterpulsing characteristics showed a characteristic time of approximately

90 ns and an afterpulsing probability of less than 1%. The device operates with a low breakdown voltage of 10.26 V and a small excess bias of 0.75 V. As proof of concept, three-dimensional point-cloud images were successfully captured using the direct time-of-flight technique.

The recent discovery of new low-dimensional materials [40] has opened new perspectives in this field thanks to the high mobility of the charge carriers, the variable electronic bandgap, suitable for a wide wavelength range, and their crystalline structure that allows them to be integrated with other elements, first of all, silicon [41]. The latest generation of these materials, the van der Waals structures, are particularly suitable to be integrated with Si devices as the weak atomic bonds that connect the various crystalline planes allow them to adapt to different types of crystals. They showed the widest electronic properties going from metallic to semiconducting and insulating up to topological insulators. Some of them, such as black phosphorus (BP) [42] or Transition Metal Dichalcogenides (TMD) [43], have received great attention in the recent past thanks to particular properties such as variable gap according to thickness (BP) or good compatibility with class III-V semiconductors (TMD). Others, like hexagonal Boron Nitrate (h-BN), show insulating behavior useful for possible separation in integrated circuits [44]. Almost all 2D materials can be synthesized at low cost with thickness as low as a few unit cells, preserving their electronic characteristics. Moreover, thanks to their van der Waals nature and the absence of surface dangling bonds, they can be easily combined to obtain new artificial materials with desired electronic and optical properties [43]. The most successful approach as detectors consists of the combination of two or more low-dimensional materials with the aim to take advantage of the properties of each of them. In this view, the charge transport mechanism and the band alignment can be optimized to improve the performance of the device, while the integration of materials with different bandgaps leads to broadband photodetectors. As an example of combination, PbS [45], PbSe [46], and HgTe [47] QDs are usually used as broadband light absorbers and deposited on the surface of a high mobility 2D-material as graphene. The photocharges generated after light absorption are transferred to the high mobility layer and delivered to the external circuit. This method allows the obtaining of responsivity as high as 10^7 A/W at 1450 nm for graphene/PbS QDs structures [45]. Different mechanism based on the formation of p-n heterojunctions between MoS_2 and BP shows specific detectivity of 10^9 cm. $\sqrt{H_z}$/W at 1550 nm [48]. Similar results are obtained for $PtSe/CdTe$, $PtSe_2/PtS_2$, $WSe_2/SnSe_2$, $MoSe_2/WSe_2$, MoS_2/WSe_2, $MoS_2/MoTe_2$ [49]. Other interesting materials showing promising perspectives in SPD are topological insulators [50]. These represent a new state of matter showing high mobility helical Dirac states on the surface, which are protected by time-reversal symmetry. The bulk of these materials is semiconducting with electronic bandgap in the range of hundreds of *meV*. For their properties, they can be used with the double function of infrared absorbers and high mobility layers. Moreover, the helical nature of the surface electrons, which lock their momentum with their spin, makes these materials suitable for polarized light detection [51]. Although very promising, low-dimensional materials still suffer from grain boundary and growth defects, which limits their charge mobility [52]. This limit, known since the first attempts of graphene synthesis, is difficult to overcome for large-area devices and can be reduced only using expensive and sophisticated fabrication methods such as molecular beam epitaxy (MBE) [53]. Table 3 compares the advantages and limitations of common low-dimensional materials used in SPADs.

Table 3. Advantages and limitations of low-dimensional materials used in SPADs.

	Advantages	Limitations
Graphene	- Extremely high carrier mobility supports fast avalanche response times. - Broad spectral responsivity (visible to terahertz) enables wide-range photon detection. - Flexible and compatible with silicon and CMOS technologies. - Robust under high electric fields needed for SPAD operation.	- Zero-bandgap results in low avalanche multiplication efficiency unless paired with other materials. - Requires complex heterostructures or doping to create the electric fields necessary for avalanche multiplication. - High dark current due to lack of bandgap increases noise. - Susceptible to environmental degradation; requires encapsulation.
TMDs (MoS_2, WSe_2, …)	- Direct bandgap in monolayers enables efficient photon absorption and avalanche multiplication. - Strong excitonic effects enhance interaction with photons, improving detection efficiency. - Spectrally tunable properties based on material and layer number make them adaptable to specific photon energies. - Easier to achieve low dark current compared to graphene due to the presence of a bandgap.	- Moderate carrier mobility compared to graphene limits response speed. - Thin layers may lead to limited absorption; requires thicker or multilayer structures for higher efficiency. - Fabrication variability affects the reproducibility of SPAD performance. - Low thermal stability under high biases can limit operational robustness.
Phosphorene	- Tunable bandgap (0.3–2 eV based on thickness) allows detection from visible to near-infrared wavelengths. - High anisotropy can enable polarization-sensitive single-photon detection - Strong photon absorption enhances SPAD sensitivity in the infrared.	- Highly reactive with oxygen and moisture, requiring strict environmental controls and encapsulation - Lower carrier mobility compared to graphene reduces response speed in avalanche regimes. - Synthesis challenges and layer control affect device consistency.
Boron Nitride (h-BN)	- Wide bandgap ($\sim$6 eV) provides excellent electrical insulation, reducing crosstalk in SPAD arrays. - Exceptional thermal and electrical stability supports high-bias operation in SPADs. - High-quality heterostructures can be formed when combined with other 2D materials.	- Not intrinsically photoresponsive; must be paired with active materials like TMDs or graphene for photon detection. - Limited optical absorption makes it unsuitable as a standalone active layer. - Serves more as a supporting material than an active photodetector
Carbon Nanotubes (CNTs)	- High aspect ratio and localized field effects support avalanche processes at nanoscale junctions. - Strong absorption of photons can trigger efficient avalanche multiplication in nanostructured designs - Chirality-dependent properties make uniform device fabrication challenging.	- Electrical noise from metallic CNTs reduces signal fidelity in avalanche multiplication. - Ultrafast carrier dynamics enable fast response in avalanche regimes. - Poor scalability compared to planar materials like TMDs and graphene

Quantum Dots (QDs)	- High quantum efficiency and size-tunable bandgap allow operation over a wide spectral range. - Can be integrated into SPAD designs to enhance light absorption and create local avalanche regions - Compatible with flexible and transparent SPAD designs.	- Susceptible to photobleaching and degradation over time. - Slow carrier dynamics compared to 2D materials limit speed in SPAD applications. - Limited scalability and difficulty in uniform integration into planar SPAD.

In devices studied in [54], the Colloidal QD solids give rise to external quantum efficiency greater than 80% at 1550 nm, a measured detectivity of 8×10^{11} Jones, and a 10-ns response time.

1D quantum nanowires are another low-dimensional material system showing superior single-photon detection performance [55–57]. The structures using nanowires or nanobelts can be fabricated in much less expensive systems with respect to MBE (about a factor of 100 in purchase and maintenance costs), and in a shorter time [58]. Compared to polycrystalline films, nanowires or nanobelts present some interesting advantages, such as the superior crystal quality that can minimize the impurities density, the deleterious effects of defects, and grain-boundary recombination, thus contributing to the high sensitivity of the device; the larger built-in electric field at the heterostructure interface that prolong the carrier lifetime and greatly reduces the transit time of photon-generated carriers in the device, leading to the high sensitivity and fast response of the device; the low reverse breakdown voltage of the order of a few volts in nanowire-nanobelt/Si junctions which is favored by the nanoscopic size where high electric fields are generated. This makes nanowires or nanobelts excellent candidates for low-power avalanche photodetectors, the basic unit of SPAD. Further optimization of the response of the device can come from the use of nanobelts instead of nanowires. These have a flattened shape, compared to cylindrical nanowires, and can offer greater adhesion to the surface of the Si substrate, onto which they are transferred for Si/nanobelt heterojunction formation. Si/nanobelt heterojunctions are obtained using Bi_2Te_3 topological insulators as in Refs. [59–61].

On the other hand, the study reported in Ref. [62] investigates the discovery and origin of one-dimensional (1D) moiré stripes on the surface of Bi_2Se_3 topological insulator (TI) thin films and nanobelts. Through scanning tunneling microscopy (STM) and high-resolution transmission electron microscopy (TEM), the researchers observed a unidirectional strained top layer with a deformation ranging from 14% to 25% compared to the relaxed bulk structure. This strain was not attributed to substrate lattice mismatch but rather to a specific growth mechanism. HRTEM micrograph and the FFT of the surface of Bi_2Se_3 sample are shown in Figure 2. The 1D stripes exhibited a spatial modulation of the local density of states, showing a significant enhancement compared to the bulk system. Density functional theory (DFT) calculations aligned with the experimental findings, confirming the preservation of the TI surface Dirac cone in the 1D moiré stripes, as expected from the material's topology. However, a substantial renormalization of the Fermi velocity was noted, and this velocity varied between the top and valley of the stripes. The markedly increased density of surface states in the 1D moiré superstructure of the TI was identified as having the potential to induce strong correlations in the topological surface states. These correlations could, in turn, lead to phenomena such as surface magnetism and topological superconductivity. The research sheds light on the intricate interplay between strain, surface morphology, and electronic properties in topological insulators, offering insights into potential applications and emergent phenomena in these materials. InP nanowire

arrays gave more interesting results with high gain beyond 10^5 and 0.8 quantum efficiency in the whole visible-wavelength range [57].
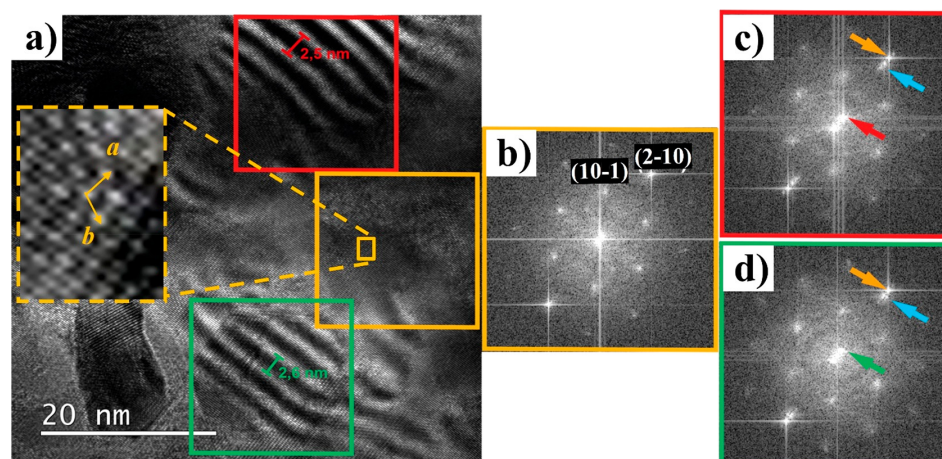

Figure 2. One-dimensional (1D) moiré stripes on the surface of Bi_2Se_3 topological insulator (TI) nanobelts (**a**) HRTEM micrograph of the surface of a Bi_2Se_3 nanobelt. Three squares highlight two regions with stripes and one without any features as a reference. The dashed box shows an atomic resolution of the region without stripes. (**b**) FFT of the region with no moiré fringes corresponding to the monocrystalline Bi_2Se_3. (**c,d**) FFT shows new features marked by arrows. Red and green arrows indicate the 2.5 and 2.6 nm periodicities of moiré stripes, respectively. The orange arrow indicates the spot corresponding to the (2–10) interplanar distance, while blue arrows indicate a direct lattice strain along the (2–10) direction [62].

The avalanche effect in 2D materials, particularly in van der Waals heterostructures, has become a subject of significant interest in the electronics and optoelectronics community. This interest was sparked by the successful isolation of 2D graphene in 2004 [63–66], which led to a surge of exploration into other 2D materials. Transition metal dichalcogenides (TMDs) [67–70], black phosphorus (BP) [71–75], and hexagonal boron nitride [76–78] are among the many 2D materials that have been intensely studied for their potential applications in electronics and optoelectronics. 2D graphene, a carbon allotrope arranged in a flat monolayer with a honeycomb lattice structure, exhibits a zero-bandgap nature. This means it has degenerate conduction and valence bands at the six corners of the Brillouin zone. While this gapless property allows graphene to interact with light across a wide spectrum from ultraviolet to microwave [66,79], making it promising for broadband photodetection, it poses challenges for achieving high signal-to-noise ratios in photodetectors. In contrast, other 2D materials like TMDs [42,63,67,68,80–83] and BP [71–75], which have decent bandgaps, have become attractive options for photodetection applications. 2D graphene field-effect transistors demonstrate ultrahigh room-temperature mobility, reaching up to 15,000 cm^2 V^{-1} s [65,84]. However, the zero-bandgap nature of graphene prevents the realization of photodetectors with a high signal-to-noise ratio [85]. The unique properties and wide range of material characteristics in 2D materials, combined with the possibilities offered by van der Waals hybrids of these materials [44,86–89], open up avenues for creating a variety of ultrasensitive photodetectors.

Conventional APDs typically require high voltage to initiate impact ionization of avalanche breakdown. This is due to their long active regions, which are on the micrometer scale, hindering carrier multiplication with high gain, low bias, and superior noise performance [90]. However, in nanoscale InSe/BP 2D/2D heterostructures, the active region is significantly shorter, falling within the sub-mean free path region. This characteristic enables these heterostructures to achieve what is known as ballistic avalanche [91]. In a vertical InSe/BP 2D/2D heterojunction, both the InSe and BP layers have thicknesses of approximately 10 nm.

The BP layer is positioned directly on top of the InSe layer to create a vertical structure. In this setup, the 2D BP layer serves as the avalanche region, which can be effectively modulated by an external electric field. The ultrashort nature of the avalanche region in these structures results in high carrier multiplication, reaching up to 3×10^4, along with superior noise performance. Due to their atomically thin nature, 2D layered materials often exhibit low-light absorption coefficients. However, employing impact ionization, which supports carrier multiplication, presents a promising approach to designing 2D photodetectors with high gain [86,91,92]. Despite this potential, avalanche photodetectors based on 2D materials and their van der Waals heterostructures have not been extensively studied. Therefore, this area holds significant promise as a research direction within the 2D optoelectronics community, especially for advancements in single-photon detection technologies.

3.2. Superconducting Nanowire Single-Photon Detector (SNSPD)

SNSPD [93] is a completely different approach. In these materials, electrons couple in a Bosonic condensed state below the critical temperature T_c. The condensed state is separated by an energy gap from the normal state that, for most superconductors, is of the order of a few *meV*. The operation principle of these devices is based on the transition to the dissipative normal state when incident radiation with energy of the same order of the superconducting gap interacts with the superconducting nanowire cooled below T_c. The nanowire is DC-biased at a value just below its critical current density value J_c. The interaction with a photon of a given energy generates a hotspot, which reduces the superconducting cross-section, forcing the bias current to flow across a thinner section of the nanowire around the hotspot region. This increases the current density flowing in the nanowire at a value higher than the critical value J_c, inducing the transition to the normal state. Consequently, an increase in the voltage is recorded depending on the normal state resistance of the nanowire. The choice of the material affects the working temperature, the bias current as well as the size of the nanowire [93]. This last condition is bound to the dimension of the hotspot generated after the absorption of the photon, which depends on the coherence length ξ of the superconducting material. The best requirements are high T_c to reduce time and consumption related to the cooling process, high normal state resistivity ρ, to have a detectable voltage signal, and sizes of 2–3 times ξ. Commercial SNSPD is mainly made of NbN, a superconducting material with $T_c = 15$ K, J_c of the order of 10^8 A/cm^2, $\xi = 5$ nm and $\rho = 20$ μΩ · cm. Other materials are Nb ($T_c = 9.2$ K), NbTiN ($T_c = 11.8$ K, $\rho = 156$ μΩ · cm), TaN ($T_c = 8.7$ K, $\rho = 250$ μΩ · cm). Despite the inconvenience of the cooling process, which limits this kind of detector to a few applications, SNSPD shows many advantages. These come from their high efficiency related to the transition to the superconducting state, which gives an output signal of hundreds of *mV* detectable without the use of amplifier circuits; to the absence of quenching circuits because the operation conditions are restored by the cooling mechanism; to possible large area obtained by shaping the nanowire in the form of meander; very low noise, due to the reduction of heating effects in the superconducting state. Other materials with higher T_c are experimented for SNSPD [94]. They are high-temperature superconductors such as YBCO, PrBCO, etc., with $T_c = 92$ K and $J_c = 10^7$ A/cm^2. However, despite the advantage of working at higher operation temperatures, these materials suffer from the presence of thermal fluctuations, which strongly affect their stability when biased below the critical current.

SNSPDs have been recently implemented in two different schemes to demonstrate devices with some photon-number-resolving capability. Both achieve this using several distinct nanowires to fill the active area rather than just a single nanowire. The first scheme, known as the parallel-superconducting Nanowire Single-Photon Detector (P-SNSPD) [95], utilizes nanowires connected electrically in parallel. The currents flowing through these parallel wires are combined, generating a single analog output signal proportional to the number of wires that have transitioned to the normal state due to incident photons. This configuration offers the potential for even faster operation compared to the original single SNSPD, as the inductance of individual wires is much lower than the longer single-wire meander of the original SNSPD, which was limited by inductance in its temporal response [96]. This parallel-SNSPD design has been demonstrated using niobium nitride (NbN) nanowires with a width of 100 nm, capable of counting up to four photons. It exhibits a low dark-count rate of 0.15 Hz and operates at a high repetition rate of 80 MHz.

In the work described in Ref. [97], they implemented a novel and simple scheme that can read out multiple SNSPDs with only one coaxial cable without the requirement of complex post-processing. Figure 3(Left) illustrates the final device setup, comprising four SNSPDs and two alignment mirrors, with a fixed 127 μm spacing to align with the fiber-to-fiber pitch of a six-channel fiber array (FA) made of standard single-mode fibers (SMFs). Alignment is conducted at room temperature by reflecting light from the substrate surface through the first and sixth fibers and optimizing their position over the Au mirrors using a power meter. Once aligned, the FA is secured to the sample with cyanoacrylate adhesive (inset, Figure 3(Right)). The sample is then mounted in a GM cryostat (Figure 3(Right)) and cooled to a base temperature of 2.9 K. Combining their approach with the use of a cryogenic amplifier, tens of detectors can be read with a single coaxial cable with a minimum thermal impact on the operating temperature. Although the parallel-SNSPD performs well in terms of dark-count rate and repetition rate, its detection efficiency at 1300 nm is relatively modest at 2%, lagging behind other photon-number-resolving detectors in this specific aspect [95].
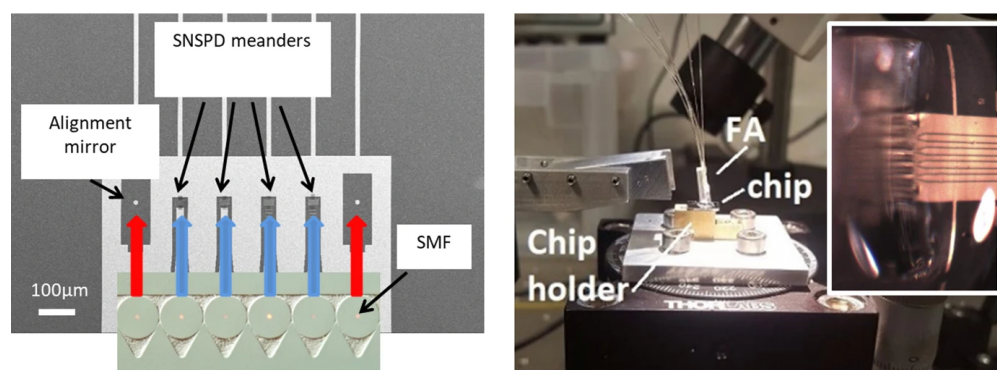

Figure 3. (**Left**): Scanning electron microscopy of the sample layout showing two alignment mirrors and four SNSPDs. In the image is illustrated the end face of the six-channel FA used for the coupling. The first and sixth fibers (red arrows) are used to locate the position of the Au mirrors. (**Right**): Sample holder with the FA glued and top and ready to be mounted on the cold head of a GM cryostat. (**Inset**): Optical microscope picture of the FA glued to the sample [97].

The study in [98] presents an experimental approach to evaluate the detection latency in SNSPDs, highlighting that low-latency materials are critical for minimizing timing jitter. Using a tailored NbN SNSPD, whose optical micrograph illustrated in Figure 4, the authors demonstrate exceptional temporal resolution, achieving 2.6 ± 0.2 ps for visible wavelengths and 4.3 ± 0.2 ps at 1550 nm. These findings underscore the importance of material properties in optimizing SNSPD performance for high-precision applications.
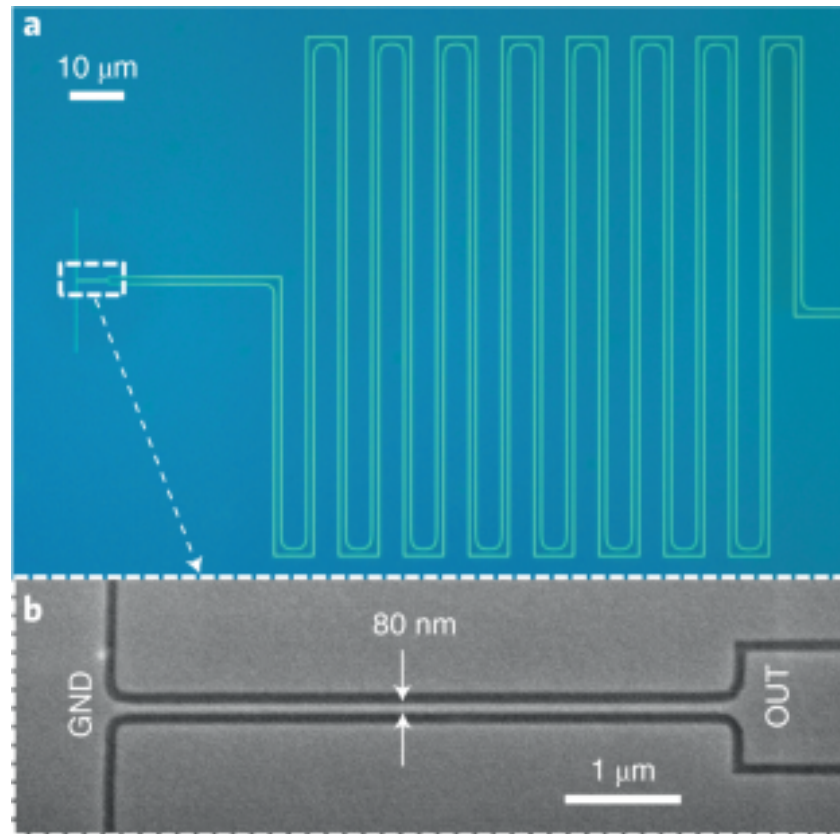
Figure 4. Low-jitter specialized niobium nitride SNSPD. (**a**) Optical micrograph of a representative device. with a small dashed rectangle on the left showing the nanowire region. Darker blue represents the NbN, while the lighter green/blue color represents the regions removed in the CF4 etch. (**b**) The nanowire region [98].

The research in [99] explores the fabrication of two types of high-temperature superconducting nanowires for single-photon detection. The photon count rate exhibits linear scaling with radiation power at the telecommunications wavelength of 1550 nm, confirming single-photon operation. High-temperature SNSPDs are fabricated by transferring 10–15 nm BSCCO flakes onto pre-patterned gold contacts, encapsulating them with hBN slabs to prevent degradation, and patterning meander structures using a He+ ion beam, which introduces insulating regions without etching (Figure 5a,b). The resulting SNWs are 56 μm long and 100 nm wide (Figure 5b inset). To enable scalable production, LSCO-LCO bilayer films (Figure 5c,d) are grown via atomic-layer-by-layer molecular beam epitaxy, offering high-Tc interface superconductivity, air stability, and compatibility with standard nanofabrication processes. These heterostructures support the fabrication of robust, ultra-thin SNWs. Specifically, SNSPDs fabricated from thin flakes of $Bi_2Sr_2CaCu_2O_{8+\delta}$ demonstrate single-photon response up to 25 K, while SNSPDs based on $La_{1.55}Sr_{0.45}CuO_4La_2CuO_4$ bilayer films operate up to 8 K. Although the detection mechanism remains not fully understood, the findings extend the range of materials for SNSPD technology beyond liquid helium temperatures, hinting at the potential for even higher operating temperatures with other high-temperature superconductors.
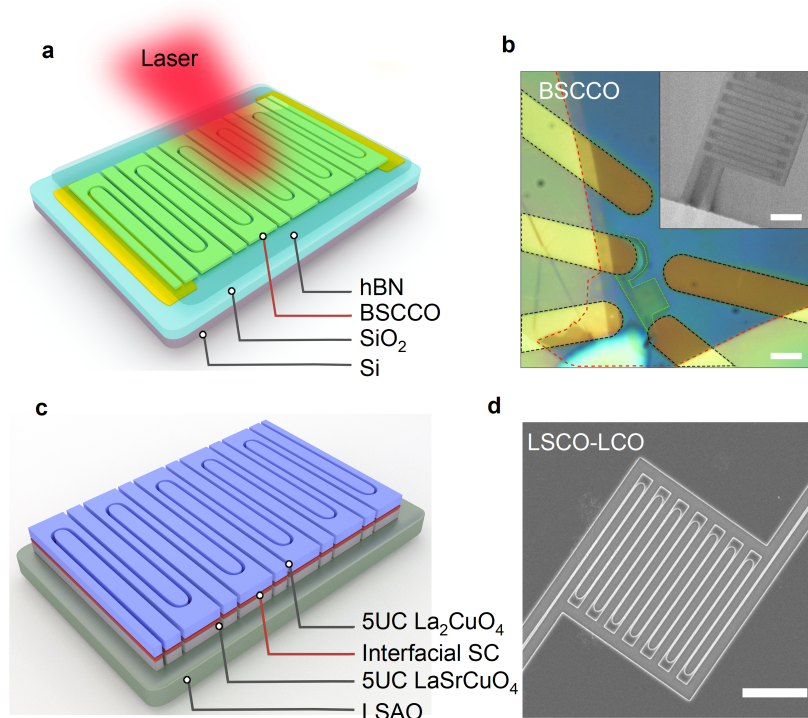
Figure 5. High temperature superconducting nanowires High-T_c superconducting nanowires. (**a**) Schematic of the BSCCO single-photon detector: a relatively thin flake of BSCCO is covered by a much thicker flake of hBN and transferred onto ultra-flat gold contacts. The SNW region is defined by a He$^+$ beam exposure. (**b**) Optical photograph of the BSCCO device. The green line demarcates the photodetector area. The contact geometry was chosen to reduce the total resistance of the gold electrodes. Scale bar, 3 μm. Inset: example SEM image of a BSCCO SNW produced by He$^+$ beam exposure. Scale bar 2 μm. (**c**) Schematic of the LSCO–LCO single-photon detector: a high-T_c two-dimensional superconductor (SC) is formed at the interface between the 5-UC-thick layer of the LCO insulator and the 5-UC-thick layer of the LSCO metal on strontium lanthanum aluminate (LSAO) substrate. The contact leads are 50 nm-thick titanium–gold. (**d**) An SEM image of a typical LSCO–LCO SNW device. Scale bar 2 μm [99].

The study presented in Ref. [100] demonstrates high-efficiency PNR detectors employing a P-SNSPD architecture. This design effectively eliminates crosstalk between pixels and is free from latching issues. The detector's behavior is modeled to predict outcomes based on a given number of incoming photons. This model is applied to a four-pixel P-SNSPD, achieving an impressive system detection efficiency of 92.5%.

In the second scheme, parallel wires are employed as completely separate detectors. Each is paired with its individual output. The resulting output is digital, wherein the number of output pulses corresponds directly to the number of photons detected. This configuration has been demonstrated using a system comprising four separate wires, achieving a reported system detection efficiency of 25% [101].

The study in Ref. [102] investigated the waveguide photon-number-resolving detectors (WPNRDs) on GaAs/Al$_{0.75}$Ga$_{0.25}$As ridge waveguides based on a series connection of nanowires. The detection of 0–4 photons has been demonstrated with a four-wire WPNRD with a single electrical readout. Waveguide-integrated WPNRDs on GaAs are fabricated through a five-step electron beam lithography process using a high-resolution Vistec EBPG 5HR system with 100 kV acceleration voltage. The first step involves defining Ti(10 nm)/Au(60 nm) electrical contact pads and alignment marks using positive-tone PMMA resist, evaporation, and lift-off. Additional Ti(5 nm)/Au(20 nm) pads are patterned

in the second step to connect nanowires to parallel resistances (yellow pads, Figure 6a inset). The WPNRD electrical structure consists of four wires connected in series, each shunted by a resistance (Figure 6b). A device quantum efficiency of ∼24% was reported at 1310 nm for the transverse electric polarization.
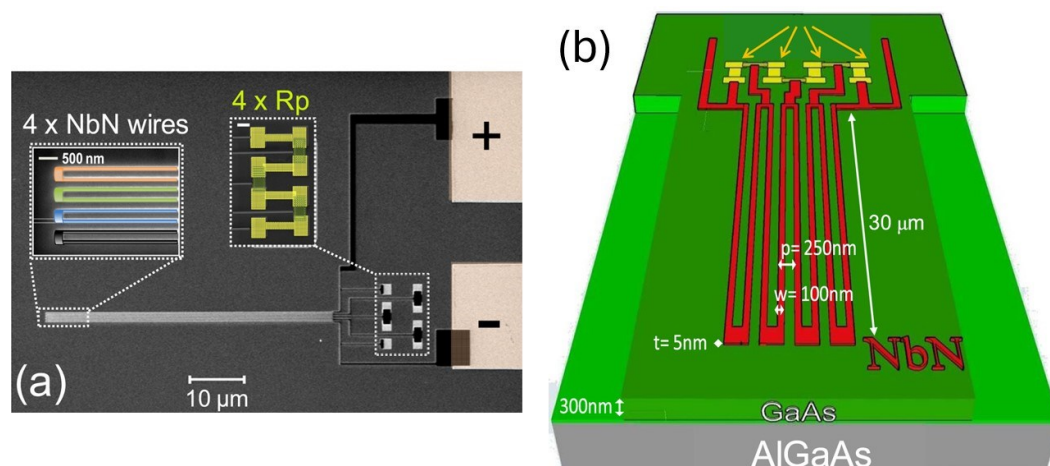

Figure 6. Waveguide photon-number-resolving detectors (WPNRDs) on GaAs/Al$_{0.75}$Ga$_{0.25}$As ridge waveguides based on a series connection of nanowires (**a**) Scanning electron microscope image of a WPNRD. Inset on the upper left: a blow-up image of the four wires before the waveguide etching step, where the wires have been colored for clarity. Inset on the upper right: a close-up, false-colored image of four AuPd parallel resistances (4 × Rp); (**b**) Schematic of a WPNRD consisting of four wires in series with a resistance (Rp) in parallel to each wire. The scale bar of both the insets is 500 nm [102].

The work in [103] introduces a compact multi-pixel SNSPD array that combines near-unity detection efficiency (91.6%), a high photon-counting rate (1.61 Gcps), a broad dynamic range capable of resolving photon numbers from 1 to 24, and four-quadrant position sensing, all integrated within a single device. The authors also constructed a communication testbed to validate the advantages of this architecture. Figure 7a displays a scanning electron microscope image of a 2 × 2 array device designed for position sensing by functioning as a photon-counting 4-QD. Each quadrant comprises six sub-pixels, with nanowires shunted by neighboring resistors arranged in a fishbone geometry (Figure 7b). This design enhances thermal cooling compared to stripline resistors, preventing latching at high counting rates. Detector fabrication details are in the supplementary materials of [104], with parameters provided in the methods section. Using 8-PPM (pulse position modulation) format communication, a maximum data rate of 1.5 Gbps was achieved, with sensitivity exceeding prior benchmarks at comparable speeds. By incorporating photon-number information into error correction codes, the receiver demonstrated robust tolerance to background noise levels of up to 0.8 photons/slot at a data rate of 120 Mbps, indicating suitability for daylight operation. Preliminary beam tracking tests using open-loop scanning further revealed quantitative sensitivity variations based on beam location, emphasizing the system's adaptability and potential for advanced applications.
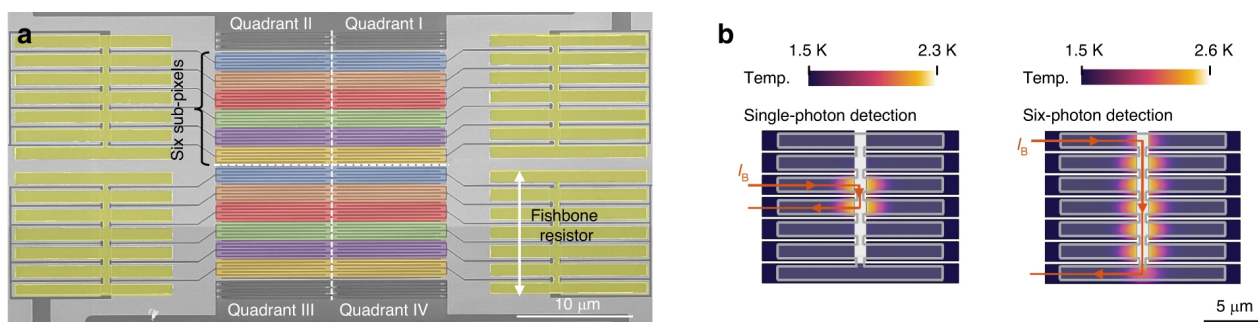
Figure 7. Detector architecture. (**a**) Scanning electron microscope (SEM) image of the 4-QD. (**b**) Simulations of the temperature distribution of the niobium nitride (NbN) surface below the "fishbone" resistor when the third sub-pixel fires and all six sub-pixels fire [103].

3.3. Quantum-Dot Field-Effect Transistor-Based Detector (QDOGFET)

QDOGFET [104–106] is a novel single-photon detection method developed for near-IR sensitivity. This design incorporates a QD with a field-effect transistor (FET) to create a highly sensitive photon detector. The QDOGFET structure consists of an optical absorber with a thin layer of QDs placed between the gate electrode and the FET's conduction channel. In this setup, incident photons are absorbed, and the resulting charges move to the QDs, where they are trapped. These trapped charges shield the gate potential, altering the FET's channel conductance. In specific implementations, trapped carriers, such as holes, reduce the negative field of the QDs, enhancing device conductivity [107]. This configuration enables unimpeded current flow until the photon-generated carrier is removed or recombined, producing an observable single-photon signal. Another variation of this detector operates similarly but uses native traps instead of QDs to store the photo-generated charges. Both approaches showcase innovative methods for achieving efficient single-photon detection in the near-infrared range. Ref. [108] presents ultrahigh-performance phototransistors based on a hybrid structure of $Sn_2S_6^{4-}$-capped CdSe QDs and an amorphous oxide semiconductor (AOS). The study investigates photo-induced charge separation at the interface through detailed electrochemical and spectroscopic analyses. Scanning photocurrent microscopy reveals a photovoltaic-dominated response due to the reduced density of trap states on the QD surface. Figure 8a illustrates the experimental setup for SPCM measurement. Representative photocurrent maps for SCN– and $Sn_2S_6^{4-}$-capped CdSe QD/a-IGZO phototransistors are shown in Figure 8b and c, respectively, under a drain bias of 1 V, gate bias of 0 V, excitation wavelength of 532 nm, and excitation power of 0.55 µW. These phototransistors exhibit exceptional photosensitivity (exceeding 6000 A/W), EQE of 44%, wide dynamic range, and fast response times. The findings highlight that chelating chalcometallate ligands enable superior performance in QD-based hybrid phototransistors, offering scalability and compatibility with large-scale and on-chip applications.
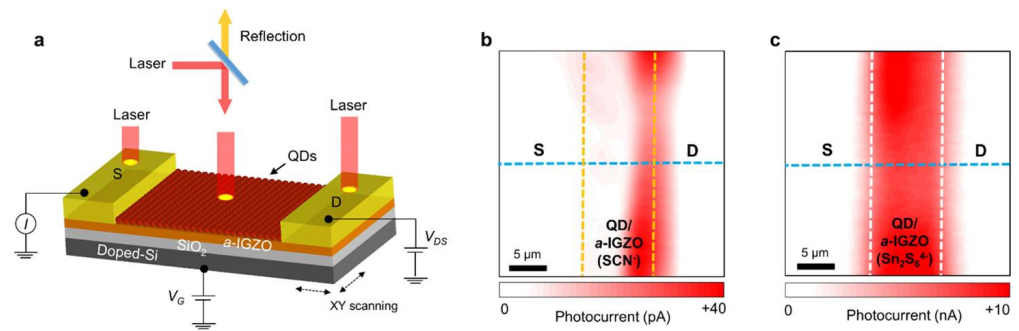
Figure 8. (**a**) Schematic of the SPCM measurement (SPCM) setup. With a laser with wavelength (λ_{laser}) of 532 nm and power of 0.55 µW. (**b,c**) Scanning photocurrent imaging in the source, channel, and drain regions (V_{DS} = 1 V) of the QD/a-IGZO phototransistor with SCN– and $Sn_2S_6^{4-}$ ligands. Scale bar 5 µm [108].

In an alternative quantum-dot-based approach, photo-generated carriers are utilized to enhance resonant tunneling through a double barrier. This method involves adjusting the electric field to align the well between the two barriers with the energy level of the band on the opposite side of one of the barriers. Consequently, the tunneling rate significantly and proportionally increases with the number of incident photons. In this scheme, the photo-generated holes trapped by the QDs play a crucial role by providing the necessary field to shift the intermediate band into resonance. This process facilitates a dramatic enhancement in the tunneling rate, making it highly responsive and efficient in detecting incident photons [109].

Depending on the specific implementation, some QD-FET detectors may exhibit photon-number-resolving (PNR) capabilities. This means they can distinguish between different numbers of incident photons. The detection efficiency of QD-FET detectors can vary depending on the specific design and materials used. The dark-count rate, which represents false counts in the absence of incident photons, is a key parameter for evaluating the performance of these detectors. The operating temperature of QD-FET detectors may vary, and some implementations may require specific temperature conditions for optimal performance.

The QDOGFET detector achieves photon-number-resolving (PNR) capability with a detection efficiency of approximately 2% at 805 nm [104–106]. It accurately distinguishes 0, 1, 2, and more than 3 photons, achieving correct assignments of 94%, 89%, 83%, and 90%, respectively, at a low dark-count probability of 0.003 per gate and a repetition rate of 50 kHz. Another QD detector, based on resonant tunneling modulation, exhibits limited PNR capability with a detection efficiency of about 0.48% [110]. A variant of this scheme demonstrates linear operation, indicating potential for PNR functionality [109]. Optimizing the dark-count rate to 200 cps reduces detection efficiency to 5%. The detector operates at 77 K, with faster performance achieved at 4 K.

3.4. Superconducting Tunnel Junction (STJ)-Based Detector

STJ-based detector [111–113] is one of the early superconducting photon-number-resolving detectors. An STJ-based detector is a type of single-photon detector that utilizes the principles of superconductivity and tunneling to detect individual photons. The key component of an STJ detector is the superconducting tunnel junction, which consists of two superconducting electrodes separated by a thin insulating barrier. The two electrodes of the tunnel junction are made of superconducting materials. When these materials are cooled below their critical temperature, they enter a superconducting state characterized by the absence of electrical resistance and the expulsion of magnetic fields. Between the superconducting electrodes, there is a thin insulating barrier. This barrier prevents the direct

flow of electrons between the superconductors but allows for quantum tunneling to occur. When a photon is incident on the detector and is absorbed, it can generate quasiparticles (excitations) in the superconducting electrodes. The generated quasiparticles can tunnel through the insulating barrier due to the quantum nature of tunneling. The tunneling current is sensitive to the presence of quasiparticles. The tunneling current is measured, and the detection of a current pulse indicates the absorption of a photon. The magnitude of the current pulse provides information about the energy of the absorbed photon.

STJ-based detectors are known for their high-sensitivity and low-noise characteristics. This device offers precise photon-number resolution, effective in the 200 nm to 500 nm wavelength range. Demonstrations have shown detection efficiencies exceeding 45%, calculated through reflectance and transmittance, at around 10 kHz count rates and 0.37 K operating temperature [113]. Background count rates are exceptionally low, below 0.1% of photo-generated counts, primarily due to electronic noise, with a minor contribution from thermal blackbody photons. The study in Ref. [114] demonstrated that cryogenically cooled, photon-counting superconducting tunnel junctions (STJs) can effectively capture optical spectra from multiple biological fluorochromes concurrently. Using a single-pixel tantalum STJ with a wavelength-resolving power of approximately $R = \lambda/\Delta\lambda = 10$, the anticipated sensitivity is confirmed to improve over traditional photomultiplier-based detectors, which are frequently used for detecting signals in microarrays and other fluorescent biological systems. This enhanced sensitivity makes STJs particularly promising for applications requiring high precision in fluorescence measurement.

Ref. [115] demonstrates single-photon detection in the near-infrared by coupling photons to localized surface plasmons within a graphene-based Josephson junction. The photon-induced switching statistics of the current-biased device reveal the pivotal role of quasiparticles generated by the absorbed photons in the detection mechanism. This approach highlights the potential for high-speed, low-power optical interconnects in future superconducting computing architectures.

3.5. Transition Edge Sensor (TES)

A TES is a type of single-photon detector that operates by exploiting the sharp change in the resistance of a superconducting material as it transitions from the superconducting state to the normal resistive state. TES detectors are highly sensitive and can detect single photons by measuring the small increase in resistance caused by the absorption of photon energy, which leads to a temperature rise in the superconducting material. This temperature change is typically on the order of millikelvins and can be detected with very high precision. TES detectors are known for their high detection efficiency (above 98%) and low dark-count rate, which makes them particularly attractive for quantum information and astronomical applications. They are especially well-suited for photon number-resolving detection, meaning they can distinguish between different numbers of photons in a single event, which is a significant advantage over traditional SPADs that typically only resolve single-photon events. The optical Ti/Au bilayer TES device reported in [116] shows an energy resolution of 0.19 eV with a $20 \times 20~\mu m^2$ active area. An antireflection structure of SiO_2 and SiN_x dielectric layers is applied to TES devices, as shown in Figure 9a, using ICP-PECVD for fabrication. Measured optical parameters at 1550 nm include refractive indices and extinction coefficients of (1.47, 0) for SiO_2, (1.92, 0) for SiN_x, (4.03, 3.81) for Ti, and (0.56, 9.91) for Au. Simulations, depicted in Fig. 3(b), show a minimum reflectivity of ~23% and transmittance near 10^{-3}. To optimize performance, 270 nm SiO_2 and 350 nm SiN_x layers are precisely deposited. Figure 9c presents the optical image of the TES device. The active Ti/Au film area, measuring $20~\mu m \times 20~\mu m$, is defined through UV lithography and a lift-off process. Nb superconducting leads, used for electrical wiring, are also fabricated via lift-off,

with sufficient thickness to preserve superconductivity during subsequent fabrication steps. Figure 9d shows the backside image captured from the CCD The devices can discriminate up to 36 photon states.
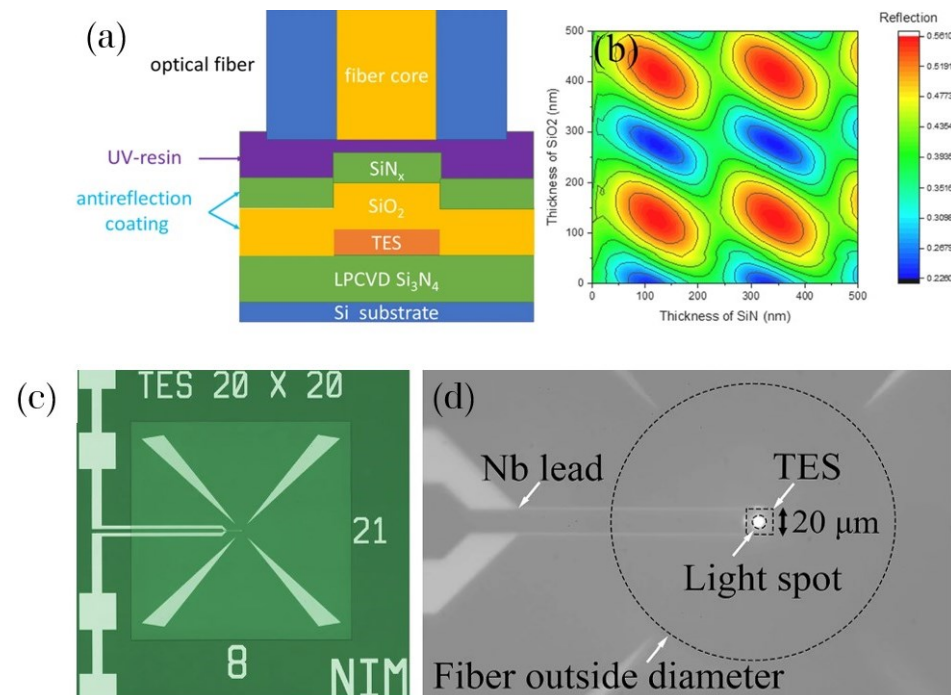

Figure 9. (**a**) The cross-section of the layer structure of the TES, including the coupled optical fiber; (**b**) simulation results of the reflectivity of the optical structure. Optical Ti/Au TES with a 20 μm × 20 μm sensitive area with Nb leads: (**c**) a whole view of the TES device; (**d**) the enlarged view of the device achieved during the optical fiber alignment process. A light spot can be observed at the center of TES to locate the position of optical fiber [116].

At visible to near-infrared (VNIR) wavelengths, Transition Edge Sensor (TES) calorimeters offer several advantages over conventional detectors, such as broad wavelength coverage, intrinsic energy resolution, high quantum efficiency, short photon detection timescales (microseconds), and negligible dark counts [117,118]. These capabilities have enabled the experimental testing of fundamental laws of quantum mechanics, particularly in loophole-free Bell tests and in photonic quantum computing. The report [119] presents an investigation into the performance of the Transition Edge Sensor (TES) when illuminated by a heavily attenuated pulsed laser operating at a repetition rate of 1 MHz. It specifically examines the effects of incorporating gold to accelerate device recovery times, utilizing a higher bandwidth readout system. The optimal performance was attained by integrating a tungsten TES with gold, which yielded a recovery time of less than 250 ns and an energy resolution of 0.25 eV full-width at half maximum at 0.8 eV photon energy.

Ref. [120] reports a significant quantum computational advantage using Borealis, a photonic processor that offers dynamic programmability across all implemented gates. Gaussian Boson Sampling (GBS) was performed on 216 squeezed modes, which were entangled with three-dimensional connectivity, utilizing a time-multiplexed and photon-number-resolving architecture. Borealis demonstrates a runtime of merely 36 μs, which represents an advantage over 50 million times more extreme than that reported from previous photonic machines. This model constitutes a substantial GBS experiment, registering events with up to 219 photons and achieving a mean photon number of 125.

Additionally, VIS-NIR TES detectors are well-suited for applications in exoplanet atmospheric spectroscopy [121,122] and biological imaging [123,124]. The current mea-

surements obtained for TES are constrained by the relatively small array sizes that have been achieved. Other limitations of TES detectors include large timing jitter and relatively long recovery times, which can hinder their use in high-speed applications like real-time quantum communication. They also require operation at very low temperatures, which necessitates complex and costly cooling systems like dilution refrigerators.

Table 4 summarizes the SPDs reported in some of the most recent articles.

Table 4. Summary of the recent SPDs.

Origin *	Year	Type	T (K)	WL (nm)	Performance
GBR [32]	2018	Ge-on-Si SPAD	125	1310	SPDE 38%, DCR 10 Mcps
CHN [33]	2022	InGaAs/InP SPAD	250	1550	SPDE 55.4%, DCR 43.8 kcps
CHN [34]	2022	InGaAs/InP SPAD	233	1550	SPDE 30%, DCR 0.665 kcps
CHE [35]	2022	InGaAs/InP SPAD	225	1550	SPDE 43%, DCR 55 kcps
GBR [37]	2024	InGaAs/AlGaAsSb APD	200	1550	SPDE 5–16%, DCR 1-20 Mcps
DEU [38]	2024	Si SPAD	200	488–532	SPDE > 6%, DCR < 100 kcps
TWN [39]	2024	Ge-Si SPAD	295	1310	SPDE 12%, DCR 19kcps
DEU [36]	2024	Ge-on-Si SPAD	110	1310	SPDE 7.3%, DCR 953 kcps
CAN [54]	2021	CQD	298	1550	EQE > 80%, Detectivity 8×10^{11} Jones, 10-ns response time
ITA [97]	2019	3C SiC SNSPD	2.9	1550	SDE 2.8%, DCR 10 kpcs
USA [98]	2020	SNSPD	295	1550	Temporal resolution 4.3 ± 0.2 ps
USA [99]	2023	$Bi_2 Sr_2 CaCu_2 O_{8+\delta}/La_{1.55} Sr_{0.45}$ CuO_4 La_2CuO_4 SNSPD	High	1550	SP response 25 K/8 K
CHE [100]	2023	P-SNSPD	0.8	1550	SDE 92.5%, DCR 140 cs
CHN [103]	2024	NbN SNSPD	295	1550	near-unity DE 91.6%, photon-counting rate 1.61 Gcps, PNR 1-24
KOR [108]	2020	$Sn_2S_6^{4-}$-capped CdSe QD/AOS	295	532	Photosensitivity > 6000 A/W, EQE 44%
USA [115]	2021	Josephson junction SPD	27 m	1550	-
CHN [116]	2022	Ti/Au TES	72 m	1550	Energy resolution 0.19 eV, Incident photon number 36
CAN [120]	2022	TES	306	1550	GBS on 216 squeezed modes in 36 μs, Mean photon number 125
USA [119]	2023	Ti/Au TES	45 m	1550	Recovery time < 250 ns, Energy resolution 0.25 eV

WL: wavelength; SPDE: single-photon detection efficiency; DCR: dark-count rate; CQD: colloidal quantum dot; QD: quantum dot; EQE: external quantum efficiency; SDE: system detection efficiency; PNR: photon number resolving; AOS: amorphous oxide semiconductor; *: country code Alpha-3.

4. Conclusions

In the field of single-photon detectors, although SPADs are widely utilized for numerous applications, specific needs often demand capabilities beyond what SPADs can offer individually. Consequently, extensive research efforts focus on enhancing detectors, targeting various improvements such as achieving nearly 100% detection efficiencies, reducing timing jitter to sub-50 picoseconds, mitigating afterpulsing effects, and improving photon-number resolution. Table 5 compares the different types of SPD introduced in this article: SPADs, SNSPDs, QD-FET-based detectors, and STJ-based detectors, highlighting their key characteristics and typical applications.

Simultaneously, researchers are exploring multifaceted approaches to enhance multiple detector parameters concurrently. For instance, advancements are underway to impart photon-number resolution to high-speed SNSPD systems by employing multiple-element detectors. Innovations, like switched multiplexed detectors, aim to reduce both dead time and afterpulsing effects simultaneously. Moreover, inventive techniques like infrared up-conversion schemes are being investigated, exhibiting high efficiency, elevated count rates, and minimal background noise. SPDs are a rapidly evolving field due to their critical role in quantum technologies, optical communication, and advanced sensing applications. The detection and manipulation of single photons are essential for a range of applications in quantum information science, including quantum computing, secure QKD in cryptography, and quantum-enhanced metrology. Here are some key trends in this area:

Advances in SNSPDs

- SNSPDs are among the most promising single-photon detectors due to their high efficiency (over 90% in some cases), low timing jitter (tens of picoseconds), and excellent scalability.
- They operate at cryogenic temperatures but offer unrivaled performance for quantum communication, deep-space optical communication, and other high-precision applications.
- Research is focusing on increasing their detection efficiency across a broader range of wavelengths and reducing cooling requirements, potentially making them more commercially viable.

Photonic Integrated Circuits (PICs) for Single-Photon Detection

- Integrating SPDs directly onto photonic chips is a growing trend, supporting scalable quantum computing and communications.
- This trend involves developing on-chip SNSPDs, APDs, or other quantum detectors, allowing for more compact, robust, and efficient quantum circuits.

Single-Photon Detectors for QKD

- The development of highly efficient, low-noise single-photon detectors is central to advancing QKD systems for secure communication.
- Optimizing SPDs for use in both terrestrial and satellite-based QKD networks is an area of intense research, requiring detectors capable of high-speed operation with low error rates.

Room-Temperature Detectors

- Efforts are ongoing to develop room-temperature single-photon detectors using novel materials such as 2D materials (graphene, MoS_2, etc.) and nanostructured semiconductors. These detectors aim to combine high efficiency with the practicality of not requiring complex cooling systems.

Improvement in Timing Resolution

- Timing resolution (jitter) is crucial for TCSPC applications and quantum information processes. Research is driving towards detectors with increasingly precise time resolution, pushing sub-10 picosecond jitter in some cases.

Applications in Quantum Sensing and Imaging

- SPDs are being adapted for quantum-enhanced sensing applications such as quantum LiDAR, where they offer superior depth resolution, and in quantum-enhanced microscopy and imaging systems, leveraging their high sensitivity.

Cryogenic Systems and Detector Packaging

- Making SPDs more practical involves not only improving intrinsic properties but also designing efficient cryogenic systems and compact packaging that can interface seamlessly with quantum systems.

Single-photon detectors face several challenges that must be addressed to fully realize their potential. One major issue is the trade-off between detection efficiency and noise levels, as higher efficiency often increases dark counts. This can be mitigated by developing advanced quenching circuits and noise-suppression techniques. Another challenge is the reliance of some SPDs, like SNSPDs, on cryogenic cooling, which adds complexity and cost; exploring high-critical-temperature superconductors or alternative cooling methods could offer a solution. Integration with existing optical and quantum systems is also challenging due to mismatched interfaces and sizes, requiring compact designs and hybrid integration technologies. Scalability for large-scale quantum networks poses thermal and power constraints, which could be addressed through multiplexing and efficient thermal

management. SPDs also struggle with sensitivity across a broad wavelength range, which might be overcome by multi-junction or spectrally adaptive designs. Lastly, achieving better timing resolution while maintaining high efficiency is technically complex but could be advanced through optimized geometries and sophisticated signal processing techniques.

Table 5. Comparison table of SPADs, SNSPDs, QD-FET-based Detectors, STJ-based Detectors and TES Detectors.

Type	Advantages	Limitations	Typical Applications
SPAD	Room-temperature operation; compact; high-speed response; scalable for arrays.	Limited detection efficiency ($\sim$50% at telecom wavelengths); higher dark-count rates.	Quantum communication, LiDAR, time-of-flight imaging.
SNSPD	Extremely low dark-count rates; high detection efficiency (>90%); low timing jitter (<50 ps).	Requires cryogenic cooling; high cost; complex setup.	QKD, quantum networks, astronomical observations.
QD-FET	Room-temperature operation; potential for integration with CMOS; broadband detection.	Still in early development; lower detection efficiency and limited photon energy resolution.	Experimental quantum optics, compact sensing devices.
STJ	Photon-number resolution; wide spectral range; negligible dark counts.	Slow recovery time; operates at very low temperatures ($\sim$100 mK).	Photon counting in astrophysics, X-ray spectroscopy.
TES	High energy resolution; photon number resolving; negligible dark counts.	Long recovery time; requires ultra-low temperatures ($\sim$100 mK).	Loophole-free Bell tests, exoplanet spectroscopy, biological imaging.

Conflicts of Interest: The authors declare no conflicts of interest.

References

1. Piergentili, P.; Amanti, F.; Andrini, G.; Armani, F.; Bellani, V.; Bonaiuto, V.; Cammarata, S.; Campostrini, M.; Cornia, S.; Dao, T.H.; et al. Quantum Information with Integrated Photonics. *Appl. Sci.* **2024**, *14*, 387. [CrossRef]
2. Amanti, F.; Andrini, G.; Armani, F.; Barbato, F.; Bellani, V.; Bonaiuto, V.; Cammarata, S.; Campostrini, M.; Dao, T.H.; Matteis, F.D.; et al. Integrated Photonic Passive Building Blocks on Silicon-On-Insulator Platform. *Photonics* **2024**, *11*, 494. [CrossRef]
3. Prete, D.; Amanti, F.; Andrini, G.; Armani, F.; Bellani, V.; Bonaiuto, V.; Cammarata, S.; Campostrini, M.; Cornia, S.; Dao, T.H.; et al. Hybrid Integrated Silicon Photonics Based on Nanomaterials. *Photonics* **2024**, *11*, 418. [CrossRef]
4. Kuhn, A.; Hennrich, M.; Rempe, G. Deterministic Single-Photon Source for Distributed Quantum Networking. *Phys. Rev. Lett.* **2002**, *89*, 067901. [CrossRef]
5. Norman, J.C.; Jung, D.; Wan, Y.; Bowers, J.E. Perspective: The future of quantum dot photonic integrated circuits. *APL Photon.* **2018**, *3*, 030901. [CrossRef]

6. Arakawa, Y.; Holmes, M.J. Progress in quantum-dot single photon sources for quantum information technologies: A broad spectrum overview. *Appl. Phys. Rev.* **2020**, *7*, 021309. [CrossRef]

7. Toninelli, C.; Gerhardt, I.; Clark, A.S.; Reserbat-Plantey, A.; Götzinger, S.; Ristanović, Z.; Colautti, M.; Lombardi, P.; Major, K.D.; Deperasińska, I.; et al. Single organic molecules for photonic quantum technologies. *Nat. Mater.* **2021**, *20*, 1615–1628. [CrossRef] [PubMed]

8. Andrini, G.; Amanti, F.; Armani, F.; Bellani, V.; Bonaiuto, V.; Cammarata, S.; Campostrini, M.; Dao, T.H.; Matteis, F.D.; Demontis, V.; et al. Solid-State Color Centers for Single-Photon Generation. *Photonics* **2024**, *11*, 188. [CrossRef]

9. Cohen-Tannoudji, C.; Dupont-Roc, J.; Grynberg, G. *Photons and Atoms: Introduction to Quantum Electrodynamics*; Wiley-Interscience: New York, NY, USA, 1997.

10. Technical Report on Quantum Cryptography Technology Experts Panel, Advanced Research and Development Activity (ARDA). 2004. Available online: http://qist.lanl.gov (accessed on 12 December 2024).

11. Ekert, A.; Gisin, N.; Huttner, B.; Inamori, H.; Weinfurter, H. In *The Physics of Quantum Information*; Bouwmeester, D., Ekert, A., Zeilinger, A., Eds.; Springer: Berlin/Heidelberg, Germany, 2000.

12. Shor, P. Algorithms for quantum computation: discrete logarithms and factoring. In Proceedings of the 35th Annual Symposium on Foundations of Computer Science, Santa Fe, NM, USA, 20–22 November 1994; IEEE Computer Society Press: Los Alamitos, CA, USA, 1994; pp. 124–134.

13. Bennett, C.; Brassard, G. Quantum cryptography: Public key distribution and coin tossing. In Proceedings of the IEEE International Conference on Computers, Systems, and Signal Processing, Bangalore, India, 10–12 December 1984; IEEE: New York, NY, USA, 1984; pp. 175–179.

14. Ekert, A.K. Quantum cryptography based on Bell's theorem. *Phys. Rev. Lett.* **1991**, *67*, 661. [CrossRef]

15. Bennett, C.H. Quantum cryptography based on Bell's theorem. *Phys. Rev. Lett.* **1992**, *68*, 3121. [CrossRef]

16. Inamori, H.; Lütkenhaus, N.; Mayers, D. Unconditional security of practical quantum key distribution. *Eur. Phys. J. D* **2007**, *41*, 599. [CrossRef]

17. Gottesman, D.; Lo, H.-K.; Lütkenhaus, N.; Preskill, J. Security of quantum key distribution with imperfect devices. *Quantum Inf. Comput.* **2004**, *4*, 325.

18. Bennett, C.H.; Brassard, G.; Crépeau, C.; Jozsa, R.; Peres, A.; Wooters, W.K. Teleporting an unknown quantum state via dual classical and Einstein-Podolsky-Rosen channels *Phys. Rev. Lett.* **1993**, *70*, 1895. [CrossRef]

19. Gisin, N.; Ribordy, G.; Tittel, W.; Zbinden, H. Quantum cryptography *Rev. Mod. Phys.* **2002**, *74*, 145. [CrossRef]

20. Rarity, J.; Owens, P.; Tapster, P. Quantum random-number generation and key sharing. *J. Mod. Opt.* **1994**, *41*, 2435. [CrossRef]

21. Stefanov, A.; Gisin, N.; Guinnard, O.; Guinnard, L.; Zbinden, H. Optical quantum random number generator. *J. Mod. Opt.* **2000**, *47*, 595. [CrossRef]

22. Li, W.; Zhang, L.; Tan, H.; Lu, Y.; Liao, S.; Huang, J.; Li, H.; Wang, Z.; Mao, H.; Yan, B.; et al. High-rate quantum key distribution exceeding 110 Mb/s. *Nat. Photonics* **2023**, *17*, 416–421. [CrossRef]

23. Grünenfelder, F.; Boaron, A.; Resta, G.V.; Perrenoud, M.; Rusca, D.; Barreiro, C.; Houlmann, R.; Sax, R.; Stasi, L.; El-Khoury, S.; et al. Fast single-photon detectors and real-time key distillation enable high secret-key-rate quantum key distribution systems. *Nat. Photonics* **2023**, *17*, 422–426. [CrossRef] [PubMed]

24. Pan, D.; Lin, Z.; Wu, J.; Zhang, H.; Sun, Z.; Ruan, D.; Yin, L.; Long, G.L. Experimental free-space quantum secure direct communication and its security analysis. *Photonics Res.* **2020**, *8*, 1522–1531. [CrossRef]

25. Bachor, H.A.; Ralph, T.C. *A Guide to Experiments in Quantum Optics*, 2nd ed.; Wiley-VCH: Weinheim, Germany , 2004; Chapter 7.

26. Siegel, P.H. Terahertz Pioneer: Jun-ichi Nishizawa, "THz Shogun". *IEEE Trans. Terahertz Sci. Technol.* **2015**, *5*, 162–169. [CrossRef]

27. Almer, O.; Tsonev, D.; Dutton, N.A.; Al Abbas, T.; Videv, S.; Gnecchi, S.; Haas, H.; Henderson, R.K. A SPAD-Based Visible Light Communications Receiver Employing Higher Order Modulation. In Proceedings of the 2015 IEEE Global Communications Conference (GLOBECOM), San Diego, CA, USA, 6–10 December 2015; pp. 1–6.

28. Yu, C.; Xu, Q.; Zhang, J. Recent advances in InGaAs/InP single-photon detectors. *Meas. Sci. Technol.* **2024**, *35*, 122003. [CrossRef]

29. Akiba, M.; Tsujino, K.; Sasaki, M. Ultrahigh-sensitivity single-photon detection with linear-mode silicon avalanche photodiode. *Opt. Lett.* **2010**, *35*, 2621. [CrossRef] [PubMed]

30. Kardynal, B.E.; Yuan, Z.L.; Shields, A.J. An avalanche-photodiode-based photon-number-resolving detector. *Nature Photonics* **2008**, *2*, 425–428. [CrossRef]

31. Chen, X.L.; Wu, E.; Xu, L.L.; Liang, Y.; Wu, G.; Zeng, H. Photon-number resolving performance of the InGaAs/InP avalanche photodiode with short gates. *Appl. Phys. Lett.* **2009**, *95*, 131118. [CrossRef]

32. Vines, P.; Kuzmenko, K.; Kirdoda, J.; Dumas, D.C.; Mirza, M.M.; Millar, R.W.; Paul, D.J.; Buller, G.S. High performance planar germanium-on-silicon single-photon avalanche diode detectors. *Nat. Commun.* **2019**, *10*, 1086. [CrossRef] [PubMed]

33. He, T.T.; Yang, X.H.; Tang, Y.S.; Wang, R.; Liu, Y.J. High photon detection efficiency InGaAs/InP single photon avalanche diode at 250 K. *J. Semicond.* **2022**, *43*, 102301. [CrossRef]

34. Zhang, B.; Yin, S.; Liu, Y.; Jiang, Z.; He, W.; Li, Q.; Hao, J.; Wang, L. High Performance InGaAs/InP Single-Photon Avalanche Diode Using DBR-Metal Reflector and Backside Micro-Lens. *J. Light. Technol.* **2022**, *40*, 3832–3838. [CrossRef]

35. Kizilkan, E.; Karaca, U.; Pešić, V.; Lee, M.J.; Bruschini, C.; SpringThorpe, A.J.; Walker, A.W.; Flueraru, C.; Pitts, O.J.; Charbon, E. Guard-Ring-Free InGaAs/InP Single-Photon Avalanche Diode Based on a Novel One-Step Zn-Diffusion Technique. *IEEE J. Sel. Top. Quantum Electron.* **2022**, *28*, 1–9. [CrossRef]

36. Wanitzek, M.; Schulze, J.; Oehme, M. Ge-on-Si single-photon avalanche diode using a double mesa structure. *Opt. Lett.* **2024**, *49*, 6345–6348. [CrossRef]

37. Taylor-Mew, J.; Collins, X.; White, B.; Tan, C.H.; Ng, J.S. Development of InGaAs/AlGaAsSb Geiger Mode Avalanche Photodiodes. *IEEE Trans. Electron. Devices* **2024**, *71*, 1994–1998. [CrossRef]

38. Govdeli, A.; Straguzzi, J.N.; Yong, Z.; Lin, Y.; Luo, X.; Chua, H.; Lo, G.Q.; Sacher, W.D.; Poon, J.K. Room-temperature waveguide-coupled silicon single-photon avalanche diodes. *npj Nanophotonics* **2024**, *1*, 2. [CrossRef]

39. Na, N.; Lu, Y.C.; Liu, Y.H.; Chen, P.W.; Lai, Y.C.; Lin, Y.R.; Lin, C.C.; Shia, T.; Cheng, C.H.; Chen, S.L. Room temperature operation of germanium–silicon single-photon avalanche diode. *Nature* **2024**, *627*, 295–300. [CrossRef] [PubMed]

40. Lemme, M.C.; Akinwande, D.; Huygheabaert, C.; Stampfer, C. 2D materials for future heterogeneous electronics. *Nat. Commun.* **2022**, *13*, 1392. [CrossRef] [PubMed]

41. Liu, Y.; Weiss, N.O.; Duan, X.; Cheng, H.-C.; Huang, Y. Van der Waals heterostructures and devices. *Nat. Rev. Mater.* **2016**, *1*, 16042. [CrossRef]

42. Chen, X.; Lu, X.; Deng, B.; Sinai, O.; Shao, Y.; Li, C.; Yuan, S.; Tran, V.; Watanabe, K.; Taniguchi, T.; et al. Widely tunable black phosphorus mid-infrared photodetector. *Nat. Commun.* **2017**, *8*, 1672. [CrossRef]

43. Liu, C.; Guo, J.; Yu, L.; Li, J.; Zhang, M.; Li, H.; Shi, Y.; Dai, D. Silicon/2D-material photodetectors: From near-infrared to mid-infrared. *Light Sci. Appl.* **2021**, *10*, 123. [CrossRef]

44. Jariwala, D.; Marks, T.J.; Hersam, M.C. Mixed-dimensional van der Waals heterostructures. *Nat. Mater.* **2017**, *16*, 170. [CrossRef] [PubMed]

45. McDonald, S.A.; Kostantanos, G.; Zhang, S.; Cyr, P.W.; Klem, E.J.D.; Levina, L.; Sargent, E.H. Solution-processed PbS quantum dot infrared photodetectors and photovoltaics. *Nat. Mater.* **2005**, *4*, 138. [CrossRef]

46. Ellingson, R.J.; Beard, M.C.; Johnson, J.C.; Yu, P.; Micic, O.I.; Nozik, A.J.; Shabaev, A.; Efros, A.L. Highly efficient multiple exciton generation in colloidal PbSe and PbS quantum dots. *Nano Lett.* **2005**, *5*, 865-871. [CrossRef] [PubMed]

47. Keuleyean, S.; Lhuillier, E.; Brajuskovic, V.; Sionnest, P.G. Mid-infrared HgTe colloidal quantum dot photodetectors. *Nat. Photonics* **2011**, *5*, 489. [CrossRef]

48. Bullock, J.; Amani, M.; Cho, J.; Chen, Y.Z.; Ahn, G.H.; Adinolfi, V.; Shrestha, V.R.; Gao, Y.; Crozier, K.B.; Chuen, Y.L.; et al. Polarization-resolved black phosphorus/molybdenum disulfide mid-wave infrared photodiodes with high detectivity at room temperature. *Nat. Photonics* **2008**, *12*, 601. [CrossRef]

49. Wang, H.; li, Z.; Li, D.; Chen, P.; Pi, L.; Zhou, X.; Zhai, T. Van der Waals integration based on two-dimensional materials for high-performance infrared photodetectors. *Adv. Funct. Mater.* **2021**, *31*, 2103106. [CrossRef]

50. Chorsi, H.; Cheng, B.; Zhao, B.; Toudert, J.; Asadchy, V.; Shoron, O.F.; fan, S.; Matsunaga, R. Topological materials for functional optoelectronic devices. *Adv. Funct. Mater.* **2022**, *32*, 2110655. [CrossRef]

51. McIver, J.W.; Hsieh, D.; Steinberg, H.; Jarillo-Herrero, P.; Gedik, N. Control over topological insulator photocurrents with light polarization. *Nat. Nanotechnol.* **2012**, *7*, 96. [CrossRef]

52. Rhodes, D.; Chae, S.H.; Palau, R.R.; Hone, J. Dosorder in van der Waals heterostructures of 2D materials. *Nat. Mater.* **2019**, *18*, 541. [CrossRef]

53. Iannaccone, G.; Bonaccorso, F.; Colombo, L.; Fiori, G. Quantum engineering of transistors based on 2D materials heterostructures. *Nat. Nanotechnol.* **2018**, *13*, 183. [CrossRef]

54. Vafaie, M.; Fan, J.Z.; Najarian, A.M.; Ouellette, O.; Sagar, L.K.; Bertens, K.; Sun, B.; de Arquer, F.P.G.; Sargent, E.H. Colloidal quantum dot photodetectors with 10-ns response time and 80% quantum efficiency at 1550 nm. *Matter* **2021**, *4*, 1042–1053. [CrossRef]

55. Natarajan, C.M.; Tanner, M.G.; Hadfield, R.H. Superconducting nanowire single-photon detectors: physics and applications. *Supercond. Sci. Technol.* **2012**, *25*, 063001. [CrossRef]

56. Luo, W.; Weng, Q.; Long, M.; Wang, P.; Gong, F.; Fang, H.; Luo, M.; Wang, W.; Wang, Z.; Zheng, D. Room-Temperature Single-Photon Detector Based on Single Nanowire. *Nano Lett.* **2018**, *18*, 5439. [CrossRef] [PubMed]

57. Gibson, S.J.; van Kasteren, B.; Tekcan, B.; Cui, Y.; Dam, D.v.; Haverkort, J.E.; Bakkers, E.P.; Reimer, M.E. Tapered InP nanowire arrays for efficient broadband high-speed single-photon detection. *Nat. Nanotechnol.* **2019**, *14*, 473. [CrossRef] [PubMed]

58. Pistawala, N.; Rout, D.; Saurabh, K.; Bag, R.; Karmakar, K.; Harnagea, L.; Singh, S. Crystal growth of quantum materials: A review of selective materials and techniques. *Bull. Mater. Sci.* **2022**, *45*, 10. [CrossRef]

59. Xiu, F.; He, L.; Wang, Y.; Cheng, L.; Chang, L.T.; Lang, M.; Huang, G.; Kou, X.; Zhou, Y.; Jiang, X.; et al. Manipulating surface states in topological insulator nanoribbons. *Nat. Nanotechnol.* **2011**, *6*, 216. [CrossRef]

60. Liu, H.; Ye, P.D. Atomic-layer-deposited Al_2O_3 on Bi_2Te_3 for topological insulator field-effect transistors. *Appl. Phys. Lett.* **2011**, *99*, 052108. [CrossRef]

61. Wang, Y.; Xiu, F.; Cheng, L.; He, L.; Lang, M.; Tang, J.; Kou, X.; Yu, X.; Jiang, X.; Chen, Z.; Zou, J.; Wang, K.L. Gate-Controlled Surface Conduction in Na-Doped Bi_2Te_3 Topological Insulator Nanoplates. *Nano Lett.* **2012**, *12*, 1170. [CrossRef] [PubMed]

62. Salvato, M.; Crescenzi, M.D.; Scagliotti, M.; Castrucci, P.; Boninelli, S.; Caruso, G.M.; Liu, Y.; Mikkelsen, A.; Timm, R.; Nahas, S.; et al. Nanometric Moiré Stripes on the Surface of Bi_2Se_3 Topological Insulator. *ACS Nano* **2022**, *16*, 13860–13868. [CrossRef]

63. Novoselov, K.S.; Geim, A.K.; Morozov, S.V.; Jiang, D.; Zhang, Y.; Dubonos, S.V.; Grigorieva, I.V.; Firsov, A.A. Electric Field Effect in Atomically Thin Carbon Films. *Science* **2004**, *306*, 666. [CrossRef]

64. Miao, J.; Zhang, L.; Wang, C. Black phosphorus electronic and optoelectronic devices. *2D Mater.* **2019**, *6*, 032003. [CrossRef]

65. Geim, A.K.; Grigorieva, I.V. Van der Waals heterostructures. *Nature* **2013**, *499*, 419. [CrossRef] [PubMed]

66. Xia, F.; Wang, H.; Xiao, D.; Dubey, M.; Ramasubramaniam, A. Two-dimensional material nanophotonics. *Nat. Photonics* **2014**, *8*, 899. [CrossRef]

67. Lee, C.H.; Lee, G.H.; Zande, A.M.V.D.; Chen, W.; Li, Y.; Han, M.; Cui, X.; Arefe, G.; Nuckolls, C.; Heinz, T.F. Atomically Thin p–n Junctions with van der Waals Heterointerfaces. *Nat. Nanotechnol.* **2014**, *9*, 676. [CrossRef]

68. Yin, Z.; Li, H.; Li, H.; Jiang, L.; Shi, Y.; Sun, Y.; Lu, G.; Zhang, Q.; Chen, X.; Zhang, H. Single-Layer MoS_2 Phototransistors. *ACS Nano* **2012**, *6*, 74. [CrossRef] [PubMed]

69. Radisavljevic, B.; Radenovic, A.; Brivio, J.; Giacometti, V.; Kis, A. Single-layer MoS_2 transistors. *Nat. Nanotechnol.* **2011**, *6*, 147. [CrossRef]

70. Das, S.; Chen, H.Y.; Penumatcha, A.V.; Appenzeller, J. High Performance Multilayer MoS_2 Transistors with Scandium Contacts. *Nano Lett.* **2012**, *13*, 100. [CrossRef] [PubMed]

71. Li, L.; Yu, Y.; Ye, G.J.; Ge, Q.; Ou, X.; Wu, H.; Feng, D.; Chen, X.H.; Zhang, Y. Black phosphorus field-effect transistors. *Nat. Nanotechnol.* **2014**, *9*, 372. [CrossRef]

72. Miao, J.; Zhang, S.; Cai, L.; Scherr, M.; Wang, C. Ultrashort channel length black phosphorus field-effect transistors. *ACS Nano* **2015**, *9*, 9236. [CrossRef]

73. Deng, Y.; Luo, Z.; Conrad, N.J.; Liu, H.; Gong, Y.; Najmaei, S.; Ajayan, P.M.; Lou, J.; Xu, X.; Ye, P.D. Black Phosphorus–Monolayer MoS_2 van der Waals Heterojunction p–n Diode. *ACS Nano* **2014**, *8*, 8292. [CrossRef]

74. Xia, F.; Wang, H.; Jia, Y. Rediscovering black phosphorus as an anisotropic layered material for optoelectronics and electronics. *Nat. Commun.* **2014**, *5*, 4458. [CrossRef]

75. Ling, X.; Wang, H.; Huang, S.; Xia, F.; Dresselhaus, M.S. The renaissance of black phosphorus. *Proc. Natl. Acad. Sci. USA* **2015**, *112*, 4523. [CrossRef]

76. Wang, L.; Xu, X.; Zhang, L.; Qiao, R.; Wu, M.; Wang, Z.; Zhang, S.; Liang, J.; Zhang, Z.; Zhang, Z. Epitaxial growth of a 100-square-centimetre single-crystal hexagonal boron nitride monolayer on copper. *Nature* **2019**, *570*, 91. [CrossRef]

77. Song, L.; Ci, L.; Lu, H.; Sorokin, P.B.; Jin, C.; Ni, J.; Kvashnin, A.G.; Kvashnin, D.G.; Lou, J. Large scale growth and characterization of atomic hexagonal boron nitride layers. *Nano Lett.* **2010**, *10*, 3209. [CrossRef] [PubMed]

78. Tran, T.T.; Bray, K.; Ford, M.J.; Toth, M.; Aharonovich, I. Quantum emission from hexagonal boron nitride monolayers. *Nat. Nanotechnol.* **2016**, *11*, 37. [CrossRef]

79. Sarma, S.D.; Adam, S.; Hwang, E.; Rossi, E. Electronic transport in two-dimensional graphene. *Rev. Mod. Phys.* **2011**, *83*, 407. [CrossRef]

80. Huang, M.; Wang, M.; Chen, C.; Ma, Z.; Li, X.; Han, J.; Wu, Y. Broadband black-phosphorus photodetectors with high responsivity. *Adv. Mater.* **2016**, *28*, 3481. [CrossRef]

81. Buscema, M.; Groenendijk, D.J.; Blanter, S.I.; Steele, G.A.; Zant, H.S.V.D.; Castellanos-Gomez, A. Fast and broadband photoresponse of few-layer black phosphorus field-effect transistors. *Nano Lett.* **2014**, *14*, 3347. [CrossRef]

82. Yuan, H.; Liu, X.; Afshinmanesh, F.; Li, W.; Xu, G.; Sun, J.; Lian, B.; Curto, A.G.; Ye, G.; Hikita, Y. Polarization-sensitive broadband photodetector using a black phosphorus vertical p-n junction. *Nat. Nanotechnol.* **2015**, *10*, 707. [CrossRef] [PubMed]

83. Wang, X.; Wang, P.; Wang, J.; Hu, W.; Zhou, X.; Guo, N.; Huang, H.; Sun, S.; Shen, H.; Lin, T. Ultrasensitive and broadband MoS_2 photodetector driven by ferroelectrics. *Adv. Mater.* **2015**, *27*, 6575. [CrossRef] [PubMed]

84. Geim, A.K.; Novoselov, K.S. The rise of graphene. *Nat. Mater.* **2007**, *6*, 183. [CrossRef] [PubMed]

85. Miao, J.; Hu, W.; Guo, N.; Lu, Z.; Liu, X.; Liao, L.; Chen, P.; Jiang, T.; Wu, S.; Ho, J.C. High-responsivity graphene/InAs nanowire heterojunction near-infrared photodetectors with distinct photocurrent on/off ratios. *Small* **2015**, *11*, 936. [CrossRef]

86. Wang, P.; Liu, S.; Luo, W.; Fang, H.; Gong, F.; Guo, N.; Chen, Z.G.; Zou, J.; Huang, Y.; Zhou, X. Arrayed van Der Waals broadband detectors for dual-band detection. *Adv. Mater.* **2017**, *29*, 1604439. [CrossRef]

87. Li, X.; Zhu, H.; Wang, K.; Cao, A.; Wei, J.; Li, C.; Jia, Y.; Li, Z.; Li, X.; Wu, D. Graphene-on-silicon Schottky junction solar cells. *Adv. Mater.* **2010**, *22*, 2743. [CrossRef] [PubMed]

88. Miao, J.; Liu, X.; Jo, K.; He, K.; Saxena, R.; Song, B.; Zhang, H.; He, J.; Han, M.-G.; Hu, W. Gate-tunable semiconductor heterojunctions from 2D/3D van der Waals interfaces. *Nano Lett.* **2020**, *20*, 2907. [CrossRef] [PubMed]

89. Liu, Y.; Huang, Y.; Duan, X. Van der Waals integration before and beyond two-dimensional materials. *Nature* **2019**, *567*, 323. [CrossRef] [PubMed]

90. Tosi, A.; Calandri, N.; Sanzaro, M.; Acerbi, F. Low-noise, low-jitter, high detection efficiency InGaAs/InP single-photon avalanche diode. *IEEE J. Sel. Top. Quantum Electron.* **2014**, *20*, 192. [CrossRef]

91. Gao, A.; Lai, J.; Wang, Y.; Zhu, Z.; Zeng, J.; Yu, G.; Wang, N.; Chen, W.; Cao, T.; Hu, W. Observation of ballistic avalanche phenomena in nanoscale vertical InSe/BP heterostructures. *Nat. Nanotechnol.* **2019**, *14*, 217. [CrossRef] [PubMed]

92. Lopez-Sanchez, O.; Dumcenco, D.; Charbon, E.; Kis, A. Avalanche photodiodes based on MoS_2/Si heterojunctions. *arXiv* **2014**, arXiv1411.3232.

93. Holtzman, I.; Ivry, Y. Superconducting nanowires for single-photon detection: Progress, challenges, and opportunities. *Adv. Quantum Technol.* **2019**, *2*, 1800058. [CrossRef]

94. Shibata, H. Review of superconducting nanostrip photon detectors using various superconductors. *IEICE Trand. Electron.* **2021**, *104-C*, 429. [CrossRef]

95. Divochiy, A.; Marsili, F.; Bitauld, D.; Gaggero, A.; Leoni, R.; Mattioli, F.; Korneev, A.; Seleznev, V.; Kaurova, N.; Minaeva, O.; et al. Superconducting nanowire photon-number-resolving detector at telecommunication wavelengths. *Nat. Photonics* **2008**, *2*, 302. [CrossRef]

96. Kerman, A.J.; Dauler, E.A.; Keicher, W.E.; Yang, J.K.W.; Berggren, K.K.; Goltsman, G.; Voronov, B. Kinetic-inductance-limited reset time of superconducting nanowire photon counters. *Appl. Phys. Lett.* **2006**, *88*, 111116. [CrossRef]

97. Gaggero, A.; Martini, F.; Mattioli, F.; Chiarello, F.; Cernansky, R.; Politi, A.; Leoni, R. Amplitude-multiplexed readout of single photon detectors based on superconducting nanowires. *Optica* **2019**, *6*, 823–828. [CrossRef]

98. Korzh, B.; Zhao, Q.Y.; Allmaras, J.P.; Frasca, S.; Autry, T.M.; Bersin, E.A.; Beyer, A.D.; Briggs, R.M.; Bumble, B.; Colangelo, M.; et al. Demonstration of sub-3 ps temporal resolution with a superconducting nanowire single-photon detector. *Nat. Photonics* **2020**, *14*, 250–255. [CrossRef]

99. Charaev, I.; Bandurin, D.A.; Bollinger, A.T.; Phinney, I.Y.; Drozdov, I.; Colangelo, M.; Butters, B.A.; Taniguchi, T.; Watanabe, K.; He, X.; et al. Single-photon detection using high-temperature superconductors. *Nat. Nanotechnol.* **2023**, *18*, 343–349. [CrossRef] [PubMed]

100. Stasi, L.; Gras, G.; Berrazouane, R.; Perrenoud, M.; Zbinden, H.; Bussières, F. Fast High-Efficiency Photon-Number-Resolving Parallel Superconducting Nanowire Single-Photon Detector. *Phys. Rev. Appl.* **2023**, *19*, 064041. [CrossRef]

101. Dauler, E.A.; Kerman, A.J.; Robinson, B.S.; Yang, J.K.W.; Voronovc, G.G.B.; Hamilton, S.A.; Berggren, K.K. Photon-number-resolution with sub-30-ps timing using multi-element superconducting nanowire single photon detectors. *J. Mod. Opt.* **2009**, *56*, 364. [CrossRef]

102. Sahin, D.; Gaggero, A.; Zhou, Z.; Jahanmirinejad, S.; Mattioli, F.; Leoni, R.; Beetz, J.; Lermer, M.; Kamp, M.; Höfling, S.; et al. Waveguide photon-number-resolving detectors for quantum photonic integrated circuits. *Appl. Phys. Lett.* **2013**, *103*, 111116. [CrossRef]

103. Hao, H.; Zhao, Q.; Huang, Y.; Deng, J.; Yang, F.; Ru, S.; Liu, Z.; Wan, C.; Liu, H.; Li, Z.; et al. A compact multi-pixel superconducting nanowire single-photon detector array supporting gigabit space-to-ground communications. *Light Sci. Appl.* **2024**, *13*, 25. [CrossRef] [PubMed]

104. Rowe, M.A.; Salley, G.M.; Gansen, E.J.; Etzel, S.M.; Nam, S.W.; Mirin, R.P. Analysis of photoconductive gain as it applies to single-photon detection. *J. Appl. Phys.* **2010**, *107*, 063110. [CrossRef]

105. Gansen, E.J.; Rowe, M.A.; Greene, M.B.; Rosenberg, D.; Harvey, T.E.; Su, M.Y.; Hadfield, R.H.; Nam, S.W.; Mirin, R.P. Photon-number-discriminating detection using a quantum-dot, optically gated, field-effect transistor. *Nat. Photonics* **2007**, *1*, 585. [CrossRef]

106. Rowe, M.A.; Gansen, E.J.; Greene, M.; Hadfield, R.H.; Harvey, T.E.; Su, M.Y.; Nam, S.W.; Mirin, R.P.; Rosenberg, D. Single-photon detection using a quantum dot optically gated field-effect transistor with high internal quantum efficiency. *Appl. Phys. Lett.* **2006**, *89*, 253505. [CrossRef]

107. Kosaka, H.; Rao, D.S.; Robinson, H.D.; Bandaru, P.; Sakamoto, T.; Yablonovitch, E. Photoconductance quantization in a single-photon detector. *Phys. Rev. B* **2002**, *65*, 201307. [CrossRef]

108. Kim, J.; Kwon, S.M.; Jo, C.; Heo, J.; Kim, W.B.; Jung, H.S.; Kim, Y.; Kim, M.; Park, S.K. Highly Efficient Photo-Induced Charge Separation Enabled by Metal–Chalcogenide Interfaces in Quantum-Dot/Metal-Oxide Hybrid Phototransistors. *Acs Appl. Mater. Interfaces* **2020**, *12*, 16620–16629. [CrossRef]

109. Blakesley, J.C.; See, P.; Shields, A.J.; Kardyna, B.E.; Atkinson, P.; Farrer, I.; Ritchie, D.A. Efficient single photon detection by quantum dot resonant tunneling diodes. *Phys. Rev. Lett.* **2005**, *94*, 067401. [CrossRef] [PubMed]

110. Shields, A.J.; O'Sullivan, M.P.; Farrer, I.; Ritchie, D.A.; Hogg, R.A.; Leadbeater, M.L.; Norman, C.E.; Pepper, M. Detection of single photons using a field-effect transistor gated by a layer of quantum dots. *Appl. Phys. Lett.* **2000**, *76*, 3673. [CrossRef]

111. Peacock, A.; Verhoeve, P.; Rando, N.; van Dordrecht, A.; Taylor, B.G.; Erd, C.; Perryman, M.A.C.; Venn, R.; Howlett, J.; Goldie, D.J.; Lumley, J.; Wallis, M. Single optical photon detection with a superconducting tunnel junction. *Nature* **1996**, *381*, 135. [CrossRef]

112. Peacock, A.; Verhoeve, P.; Rando, N.; van Dordrecht, A.; Taylor, B.G.; Erd, C.; Perryman, M.A.C.; Venn, R.; Howlett, J.; Goldie, D.J.; et al. On the detection of single optical photons with superconducting tunnel junction. *J. Appl. Phys.* **1997**, *81*, 7641. [CrossRef]

113. Peacock, T.; Verhoeve, P.; Rando, N.; Erd, C.; Bavdaz, M.; Taylor, B.; Perez, D. Recent developments in superconducting tunnel junctions for ultraviolet, optical & near infrared astronomy. *Astron. Astrophys. Suppl. Ser.* **1998**, *127*, 497.

114. Fraser, G.W.; Heslop-Harrison, J.S.; Schwarzacher, T.; Holland, A.D.; Verhoeve, P.; Peacock, A. Detection of multiple fluorescent labels using superconducting tunnel junction detectors. *Rev. Sci. Instrum.* **2003**, *74*, 4140–4144. [CrossRef]

115. Walsh, E.D.; Jung, W.; Lee, G.H.; Efetov, D.K.; Wu, B.I.; Huang, K.F.; Ohki, T.A.; Taniguchi, T.; Watanabe, K.; Kim, P.; et al. Josephson junction infrared single-photon detector. *Science* **2021**, *372*, 409–412. [CrossRef]

116. Xu, X.; Rajteri, M.; Li, J.; Zhang, S.; Pepe, C.; Chen, J.; Gao, H.; Li, Q.; Li, W.; Li, X.; et al. Investigation of Ti/Au transition-edge sensors for single-photon detection. *Low Temp. Phys.* **2022**, *209*, 372–378. [CrossRef]

117. Miller, A.J.; Nam, S.W.; Martinis, J.M.; Sergienko, A.V. Demonstration of a low-noise near-infrared photon counter with multiphoton discrimination. *Appl. Phys. Lett.* **2003**, *83*, 791–793. [CrossRef]

118. Lita, A.E.; Miller, A.J.; Nam, S.W. Counting near-infrared single-photons with 95% efficiency. *Opt. Express* **2008**, *16*, 3032–3040. [CrossRef] [PubMed]

119. Hummatov, R.; Lita, A.E.; Farrahi, T.; Otrooshi, N.; Fayer, S.; Collins, M.J.; Durkin, M.; Bennett, D.; Ullom, J.; Mirin, R.P.; et al. Fast transition-edge sensors suitable for photonic quantum computing. *J. Appl. Phys.* **2023**, *133*, 234502. [CrossRef]

120. Madsen, L.S.; Laudenbach, F.; Askarani, M.F.; Rortais, F.; Vincent, T.; Bulmer, J.F.; Miatto, F.M.; Neuhaus, L.; Helt, L.G.; Collins, M.J.; et al. Quantum computational advantage with a programmable photonic processor. *Nature* **2022**, *606*, 75–81. [CrossRef] [PubMed]

121. Rauscher, B.J.; Bolcar, M.R.; Clampin, M.; Domagal-Goldman, S.D.; McElwain, M.W.; Moseley, S.H.; Stahle, C.; Stark, C.C.; Thronson, H.A. ATLAST detector needs for direct spectroscopic biosignature characterization in the visible and near-IR. *Proc. SPIE* **2015**, *9602*, 136–143.

122. Nagler, P.C.; Greenhouse, M.A.; Moseley, S.H.; Rauscher, B.J.; Sadleir, J.E. Development of transition edge sensors optimized for single-photon spectroscopy in the optical and near-infrared. *Proc. SPIE* **2018**, *10709*, 1070931.

123. Niwa, K.; Numata, T.; Hattori, K.; Fukuda, D. Few-photon color imaging using energy-dispersive superconducting transition-edge sensor spectrometry. *Sci. Rep.* **2017**, *7*, 45660. [CrossRef] [PubMed]

124. Fukuda, D.; Niwa, K.; Hattori, K.; Inoue, S.; Kobayashi, R.; Numata, T. Confocal microscopy imaging with an optical transition edge sensor. *J. Low. Temp. Phys.* **2018**, *193*, 1228–1235. [CrossRef]